Nanostructured Non-carbonaceous Materials for Improvement of Sulfur Cathode in Lithium-Sulfur Battery

by

Quanqun Pang

A thesis

presented to the University of Waterloo

in fulfillment of the

thesis requirement for the degree of

Master of Science

in

Chemistry-Nanotechnology

Waterloo, Ontario, Canada, 2014

AUTHOR'S DECLARATION

I hereby declare that I am the sole author of this thesis. This is a true copy of the thesis, including any required final revisions, as accepted by my examiners.

I understand that my thesis may be made electronically available to the public.

Quanquan Pang

ABSTRACT

Lithium-sulfur battery based on sulfur cathode has the advantages of high specific capacity, high energy density, environmental benignity and natural abundance of sulfur. These advantages over conventional lithium-ion batteries have driven researchers to make a lot of efforts to understand the redox mechanisms and improve the cathode performance. In order to fully realize the potential of lithium-sulfur battery and to approach commercialization, there are still many problems to overcome. Among them are i) low conductivity of sulfur and the discharge product, ii) lithium polysulfide intermediates dissolution and shuttle phenomenon, iii) volumetric expansion upon discharge and iv) lithium metal dendrite formation on anode side. In this thesis, the work is mostly focused on the cathode materials in order to address the first two problems.

In the first part of the thesis, reduced titanium oxide is used as both a highly conductive support and a polysulfide adsorbent to prevent the loss of active materials. Mesoporous Magnéli phase with high surface area is synthesized through a sol-gel method. The reduction to suboxide is realized by carbothermal reaction at high temperature and the porous architecture is attributed to the cross-linking of polymer-mediated gel precursor that undergoes decomposition. The strong interaction between oxide and Li_2S_4 is confirmed by X-ray photoelectron spectroscopy analysis, based on comparison with carbon materials. This is also visually observed from a polysulfide adsorption study where the oxide and carbons were in contact with Li_2S_4 solutions. With 60 wt% of sulfur introduced onto synthesized Magnéli phase material by melt-diffusion, the cathode experienced very low capacity fading rate of 0.072% per cycle over 500

cycles at a discharge rate of 2C (full discharge in half an hour). The electrode morphology evolution upon cycling reveled by scanning electron microscopy imaging demonstrated more uniform deposition of discharge products for conductive oxide than carbon, which is due to the *in-situ* adsorption of lithium polysulfides during discharge.

In the second part, another class of metallic non-carbonaceous materials - metal boride - was explored as a sulfur host. This polar material is expected to adsorb hydrophilic polysulfide as well. Both bulk and nanosized borides were synthesized through either simple thermal decomposition of metal borohydride and solid state reaction between elements, respectively. In all samples prepared, crystalline metal boride was confirmed to be the dominant phase, with small amount of oxide forming on the surface. Especially, with the addition of carbon nanotubes for solid state reaction, the particle size of as-synthesized boride/carbon composite was effectively reduced to ~100 nm, which is vital for sulfur impregnation. With 60 wt% of sulfur impregnated, the boride/S nanocomposite exhibited a high initial capacity of 985 mA h/g_{sulfur} with only 0.1 % of capacity fading per cycle over 200 cycles at C/2.

ACKNOWLEDGEMENTS

I would like to express my gratitude to my supervisor, Professor Linda F. Nazar, for her guidance and instructions throughout my research project.

I would also like to express my gratitude to the other members of the research group, past and present, who have assisted me in research: Dr. Dipan Kundu, Dr. Marine Cuisinier, Dr. Xiao Liang, Dr. Guang He, Dr. Guerman Popov, Connor Hart, Xiaoqi Sun, Robert Black and Brain Adams.

I also acknowledge the help from Dr. Carmen Andrei from Mcmaster University on TEM imaging and Dr. Liyan Zhao from University of Waterloo on XPS data collection.

TABLE OF CONTENTS

LIST OF FIGURES

NOMENCLATURE

AC	Alternating current
BET	Brunauer-Emmett-Teller
CE	Coulombic efficiency
CNT	Carbon nanotube
CTAB	Cetyltrimethyl ammonium bromide
CV	Cyclic voltammetry
DFT	Density function theory
DME	Dimethoxymethane
DMF	Dimethylformamide
DMSO	Dimethyl sulfoxide
DOL	1,3-dioxolane
DSC	Differential scanning calorimetry
EDX	Energy dispersive X-ray spectroscopy
EIS	Electrochemical impedance spectroscopy
EV	Electric vehicles
LiPS	Lithium polysulfide
Li-S	Lithium-sulfur
LiTFSI	Bis(trifluoromethanesulfonyl)imide lithium
PANi	Polyaniline
PEG	Polyethylene glycol
PVDF	Polyvinylidene fluoride
PVP	Polyvinylpyrrolidone
QSDFT	Quenched solid state functional theory
SAED	Selected area electron diffraction

SEM	Scanning electron microscopy
TEM	Transmission electron microscopy
THF	Tetrahydrofuran
TGA	Thermal gravimetric analysis
XANES	X-ray absorption near-edge structure
XPS	X-ray photoelectron spectroscopy
XRD	X-ray diffraction

Chapter 1 Introduction

1.1 Overview of rechargeable lithium batteries

Modern civilization has positioned our planet largely dependent on combustion of fossil fuels for energy. The finite supply and uneven distribution of fossil fuel globally give rise to vulnerability of some countries as a consequence of fossil imports and competition, thus impeding the economic development.[1] On the other hand, the massive productions of CO_2 and other pollutants by combustion of fossil fuels have caused severe environmental problems, among which are global warming and air pollution.[2] Therefore, it is urgent to discover alternative sources of energy independent of fossil fuels and at the same time, replace the current internal combustion engines with electric motors.

Energy coming from solar, wind, geothermal and nuclear reaction is generally considered as promising alternatives to fossil fuels. With the development of technologies to increase energy conversion efficiencies from these sources, it is possible to reduce or even eliminate our dependence on fossil fuels. The energy thus generated is usually stored in the form of electricity via large-scale electric grid, because it is easier to transport and utilize. However, in order to use electric devices or motors on a wide scale, portable energy storage devices have to be used. Rechargeable batteries, which are usually environmentally benign, of high energy densities and low cost, become the most promising devices to store electric energy. In principle, upon charge of a rechargeable battery, the electricity is stored in the form of chemical energy and inversely, chemical energy transfers to electricity upon discharge that can be directly used for electric devices.

1.1.1 Basic Concepts

Rechargeable batteries, also known as secondary batteries can be reversibly charged and discharged for certain duration (life-time), as opposed to primary batteries (one-time use). Usually, a rechargeable battery consists of a group of electrochemical cells that are connected in series and/or in parallel to satisfy the need for desired output voltage and/or current.[3] For simplicity, most researches in the field of science are focused on improving the electrochemical performance of an individual electrochemical cell.

An electrochemical cell consists of two electrodes, cathode and anode, which are separated by an electrolyte. The operation of a cell is based in principle on the difference of chemical potentials of two active materials in electrodes, which gives rise to reduction and oxidation half reactions in cathode and anode, respectively. The electrodes should be both electrically and ionic conductive, since electron transfer and ion transportation occur on the surface and within the electrodes. The electrolyte, being an ionic conductor but electric insulator, can be either solid or liquid. An electrolyte-permeable but insulating porous separator is needed for liquid electrolyte cells.

There are some basic characteristics that are usually used when evaluating the performance of an electrode, including electrode potential, discharge/charge voltage profile, specific capacity, energy density, rate capability and cycling performance. These are essential for understanding the work in this thesis.

- The potential of an electrode is dependent on its chemical potential (*i.e.* redox potential). A large difference of potential between cathode and anode (*i.e.* voltage) is desired for a full cell, since the output power is the product of voltage and current.

The potential difference has to be within the electrochemical potential window of the electrolyte used, in order to prevent electrolyte decomposition.

- Discharge/charge voltage profile is a plot of voltage evolving as a function of specific capacity during the galvanostatic cycling of a cell, where a constant discharge/charge current is applied. The profile can explain the redox reactions and at what voltage they are happening. A plateau on the plot represents a two-phase transition reaction, whereas a slope character corresponds to a single-phase reaction. Minimum voltage difference between discharge and charge, an indicator of low degree of polarization is desired to maximize the energy efficiency.
- Specific capacity (mA h/g) or volumetric capacity (mA h/cm^3) is defined by the amount of charge (Q, mA h) stored per mass or volume of electrode for one full discharge/charge. Higher theoretical specific capacity is desired for new electrode system. Correspondingly, the energy density is the product of capacity and voltage per mass (W h/kg) or volume (W h/L).
- The current at which a cell is discharged/charged matters when considering the power density. "C/n" rate corresponds to the rate (mA/g) at which the theoretical specific capacity is achieved in n hours upon discharge. Higher rate gives higher power but normally leads to higher polarization, lower energy efficiency and lower specific capacity. High rate capability indicates the ability to maintain its capacity and degree of polarization upon increased rate.
- Cycling life usually means the capacity retention with prolonged cycle of a cell. For the commercialization of a cell, the cycle life is extremely important as it is pertinent to its actual life. In laboratory research, the test of cycle life of a cell is

usually performed by cycling a cell in a galvanostatic mode continuously until the capacity fades substantially, although in practice the discharge/charge is more complicated (*e.g.*, not always the same rate and resting periodically).

Among rechargeable batteries, lithium-based ones have become the mostly researched due to their high volumetric and gravimetric energy densities and are considered to be a promising candidate to replace nickel-based battery. Although sodium batteries are also under intensive research now and have the advantage of abundance of sodium on earth, lithium batteries seems to have a better chance to be commercialized.

1.1.2 Intercalation and integration cathodes

The cathodes of lithium batteries can be categorized into intercalation- and integration-based. Intercalation cathodes store/relieve charges via topotactic de/intercalation of Li^+ ions within the structures, whereas integration cathodes rely on integrated reaction of lithium with active materials.

First identified by Goodenough et al. in 1980, layered structured $LiCoO_2$ works as an intercalation-based active material from which Li^+ ions can be electrochemically removed/inserted in a reversible manner.[4] $LiCoO_2$-based battery was the first type of commercialized lithium-ion batteries by SONY Corporation using graphite anode and yet now is dominating the lithium battery market. More recently, olivine-structured $LiFePO_4$ has attracted more attention, because of the improved structure stability rendered by PO_4^{3-} tetrahedron and its higher theoretical specific capacity (170 mA h/g). The higher stability made it possible to exhibit very small capacity fading even after hundreds of cycles. However, the introduction of PO_4^{3-} groups in the crystal structure gives rise to its

lower electronic conductivity than $LiCoO_2$. This can be solved by fabricating nanoscaled materials and coating with conductive carbons.

Currently, conventional Li-ion batteries have enabled the commercialization of portable devices, like cell-phones, portable computers and cameras. With several decades of optimization, these batteries have virtually reached their theoretical energy density limits. However, even when fully developed, the energy storage is still too low to meet further and higher demands facing rechargeable batteries, *e.g.* from electric vehicles (EVs). New electrochemical systems with substantially higher specific capacity and energy density are desired for the next-generation batteries. Cathodes based on integrated reactions have the potential to fulfill this role. Of these, lithium-sulfur and lithium-oxygen (air) batteries based on a sulfur cathode and oxygen cathode, respectively, are the mostly defined battery system. Oxygen and sulfur are two neighboring elements in group 16 of the periodic table, and such systems operate based on the redox reaction between lithium metal and chalcogen elements. Although it seems that they have similar chemical properties, in fact they have different electrochemistry due to the different physical states and chemistry activities. [5]

Lithium-oxygen (Li-O_2) battery employs oxygen as the active agent in positive electrode and the electrochemical depends on the type of electrolyte used (i.e. aprotic or protic solvent). In an aprotic electrochemical system for example, Li_2O_2 was identified as the dominant discharge products by an nominal overall reaction $2\ Li + O_2 \rightarrow Li_2O_2$.[6] Not until recently, it was discovered that the irreversible side reactions of the intermediate superoxide O^{2-} with carbon electrode and/or carbonate-based electrolyte, not only cause irreversible formation of side products deteriorating the electrodes but also consume the

electrolyte, which made long-term full cycle impossible.[7] Dimethyl sulfoxide (DMSO) demonstrated better stability over ether-based electrolytes and the employment of metallic TiC as an electrode support has greatly reduced the side reactions and enabled an improved capacity retention over 100 cycles, although it is still unclear whether it is the surface layer of TiO_2 that accounts.[8] Redox mediators that have slightly higher redox potential than Li_2O_2 were shown to be able to reduce the polarization needed to oxidize the insulating Li_2O_2 upon charge back.[9] There is more work to be done to understand the electrochemistry and accordingly to design optimal electrode and electrolyte systems for extended cycle performance. In addition, from the view of practical applications, the sources of air or pure oxygen need to be well taken care of.

Lithium-sulfur (Li-S) battery operates based on sulfur redox reaction with lithium. This is the focus of this thesis and will be discussed in the sections below.

1.2 Lithium-sulfur battery

Sulfur has the advantages of being abundant on earth and environmental friendly, in addition to its high theoretical specific capacity of 1672 mA h/g, which is 3 – 5 times that of conventional Li-ion batteries. The specific capacity of Li-S cells is based on the mass of sulfur in cathode for this thesis.

1.2.1 Basic principles of Li-S battery

Li-S battery usually consists of a sulfur cathode, a lithium metal anode and an ether-based electrolyte. Sulfur reacts with two moles of electrons per mole of S based on an overall reaction of $S_8 + 16\ e^- \rightarrow 8\ Li_2S$. Upon discharge, the cyclo-S_8 molecule takes

electrons and Li^+ ions to form solid Li_2S, with lithium polysulfides (LiPSs, Li_2S_n, $2< n \leq 8$) of different chain lengths as intermediates, whereas upon charge, solid Li_2S is oxidized back to LiPSs and further to cyclo-S_8. It is important to note that LiPSs are readily soluble in ether-based electrolytes, while Li_2S (Li_2S_2, if exists) is not. The seemingly simple chemistry is complicated and yet to be fully understood.

The discharge/charge voltage profiles with a typical electrolyte solvent (a mixture of 1,3-dioxolane (DOL) and dimethoxymethane (DME)) are shown in bottom panel of **Figure 1.1**. [10] It is generally believed that upon discharge, the high-voltage plateau around 2.4 V corresponds to the reaction of S_8 to long-chain LiPSs (Li_2S_n,$4< n \leq 8$) and the low-voltage plateau around 2.1 V represents further reduction into short-chain LiPSs (Li_2S_n,$2< n \leq 4$) and Li_2S/Li_2S_2. Upon charge, the long gradual slope corresponds to the oxidation of solid-state Li_2S to long-chain LiPSs and the ending short plateau represents further oxidation to S_8. However, unlike the simple designation in a single-plateau profile for $LiFePO_4$, this general designation for Li-S cell has not been fully evidenced yet, by detecting all sulfur species at each stage. Nonetheless, *operando* studies on the sulfur speciation during discharge and charge via X-ray absorption near-edge structure (XANES),[10,11] UV-vis spectroscopy,[12] X-ray diffraction (XRD) and transmission X-ray microscopy [13] have provided more information on the reaction mechanism of a Li-S cell.

Our group has performed *operando* XANES study on a carbon-sulfur cathode, where four solid reference materials (Li_2S, Na_2S_4, Li_2S_6 and S_8) were successfully isolated and the weight of each sulfur compnent was determined via linear combination fit on the operando XANES spectra, as seen in upper panel of **Figure 1.1**.[10] It is observed that upon charge, Li_2S was monotonically consumed with the formation of soluble S_4^{2-}

and S_6^{2-} on the first slope stage and on the second part, S_6^{2-} and S_4^{2-} were completely converted to S_8. Upon discharge, conversion from S_8 into S_6^{2-} and S_4^{2-} ended at the supersaturation point (the knee right before second plateau), and Li_2S formation started during the second plateau and more dramatically at the end of discharge. It is worth to note that there was always a certain fraction of unutilized S_8 at all stages, which can be explained by the reaction at high-voltage plateau: $S^0 + 3/2\ Li^+ + 3/2\ e^- \rightarrow 3/4\ Li_2S + 1/4\ S^0$. The as-formed S_8 cannot be further reduced because of the sudden drop of voltage after the first plateau.[10] Other *operando* techniques have also probed the formation of sulfur and/or Li_2S, but the reactions proposed differ on different cathode structures.[13]

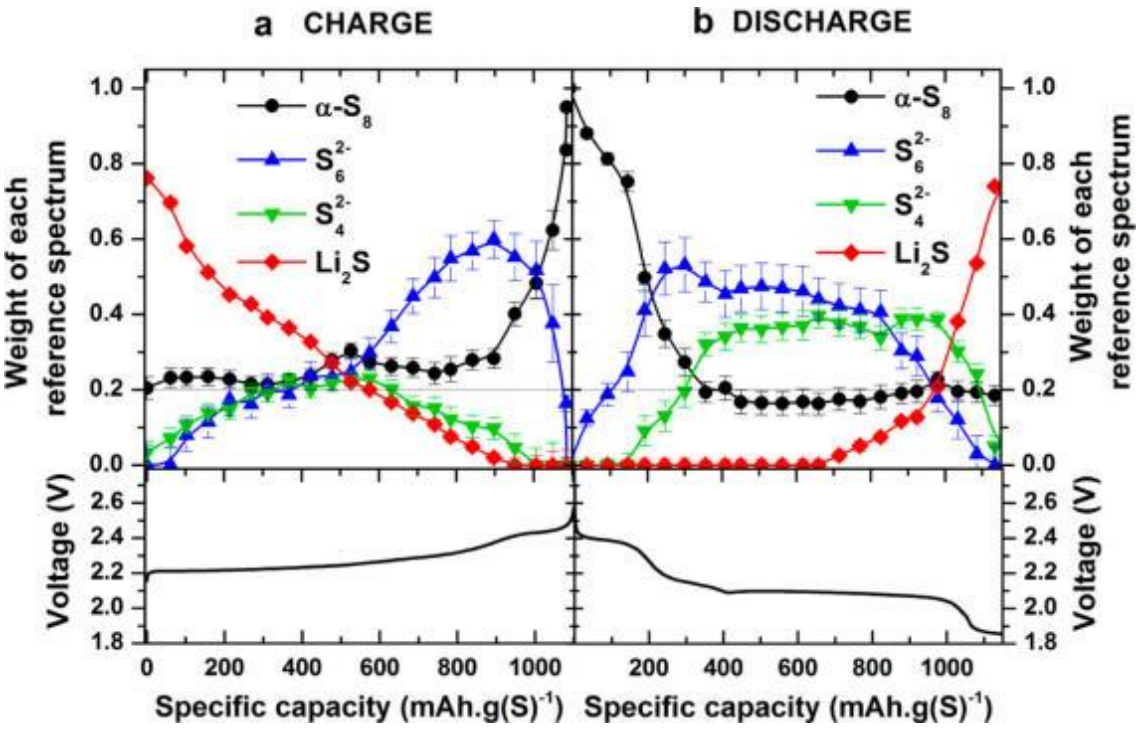

Figure 1.1 Typical voltage profile (bottom panel) and corresponding evolution of sulfur species (S_8, S_6^{2-}, S_4^{2-} and Li_2S) upon charge (a) and discharge (b) at C/10 rate. The weight of each sulfur component was determined by a linear combination fit of the *operando* XANES spectra. Reproduced from Reference 10.

1.2.2 Challenges towards Li-S battery

As mentioned above, in a Li-S cell, solid-state S_8 is reduced to soluble LiPSs with different chain-lengths and ends up forming insoluble Li_2S upon discharge and reverses upon charge. Although sulfur has a high theoretical capacity of 1672 mA h/g, the commercialization of Li-S batteries was hindered by the fact that it experienced low sulfur utilization rate, low rate capability, low Coulombic efficiency (CE) and brief cycle life, unsafe lithium metal anode, which can be attributed to the following reasons.

1.2.2.1 Physical properties of S_8/Li_2S

In a Li-S cell, the sulfur has to accept electrons from the external circuit and react with Li^+ ions, so there has to be electron transfer and Li^+ diffusion in the cathode for the reduction to occur. However, sulfur has a low electronic conductivity of only 5×10^{-30} S cm^{-1} at room temperature.[14] To solve this problem, conductive additives have to be added into the positive electrode. Carbon is currently the most widely used due to its light weight and high conductivity.[15] Since the additives lower the actual energy density of the whole cell, minimum amount of additives thus with high fraction of sulfur is desired. As well, the insoluble discharge products Li_2S_2/Li_2S are also electrically insulating. Therefore, after discharge if the products deposit on the cathode surface, the impedance and thus polarization needed to oxide Li_2S would be increased. This problem can be possibly alleviated via controlling the morphology and distribution of Li_2S. Another problem is related to the volume expansion/contraction upon Li_2S formation/consumption due to the large density difference between sulfur (2.03 g/cm^3) and Li_2S (1.67 g/cm^3). This can deteriorate the integrity of the overall electrode and further decrease the conductivity.

1.2.2.1 Polysulfide dissolution

Another major problem comes from the dissolution of LiPSs in commonly used ether-based electrolytes. During discharge/charge, the hydrophilic long-chain LiPSs can dissolve in the electrolyte and diffuse through the separator to the anode, whereupon they are reduced to solid Li_2S/Li_2S_2, forming a solid electrolyte interface layer and blocking electrolyte access to lithium metal. Continuously incoming long-chain LiPSs react with the SEI layer to form shorter-chain LiPSs, which become concentrated and thus diffuse back to the cathode and get oxidized to long-chain LiPSs. This repeated parasitic process is called the "polysulfide shuttle", which causes self-discharge and loss of active materials as well as capacity fading over cycling. Therefore, optimized control on trapping LiPSs within cathode and/or inhibiting their diffusion to anode side is critical for enhancing capacity retention.

1.2.2.3 Lithium Anode

Currently lithium metal is used as the anode in Li-S cells. However, safety can be a concern because lithium metal can readily react with any water or oxygen present in the electrolyte. In addition, dendrites are formed on the lithium surface when lithium is repeatedly stripped and plated due to the uneven distribution of current. This causes lithium metal dendrites to penetrate the electrolyte and separator causing short-circuit. Therefore, the practical application of lithium metal is largely limited. Novel anode materials with high energy density other than lithium metal are desired to marry sulfur cathode for practical applications.

1.3 Current approaches on cathode

The problem of LiPS dissolution remains to be the major issue on the cathode side. In general, the cathode consists of sulfur, a conductive additive and a polymeric binder. To be a good candidate for the sulfur cathode, the additive has to i) have a good electronic conductivity, ii) be able to host enough sulfur and iii) reduce the dissolution of LiPSs into the electrolyte.

1.3.1 Porous carbon hosts

Carbon is the most widely used material as additive. A significant improvement on the electrochemical performance of Li-S cells by our group was made by using an ordered mesoporous carbon CMK-3 with 3-4 nm pores.[15] Sulfur was impregnated into the mesopores by a melt-diffusion method, which can not only make intimate contact between sulfur and carbon to increase conductivity, but also confine sulfur and subsequent LiPSs within the pores to some extent, as shown in **Figure 1.2a**. The cathode composite with 70 wt% of sulfur exhibited an initial capacity of 1005 mA h/g at C/10 with good capacity retention over 20 cycles. Improved performance was achieved when a bimodal porous carbon was used.[16] It is believed that the smaller micropores (~2 nm) serve to trap sulfur and LiPSs during cycling while the larger pores (~5.6 nm) provide channels for electrolyte infiltration, benefiting rate capability.[16] A composite containing 50 wt% of sulfur exhibited a high capacity of 995 mA h/g with 550 mA h/g retention over 100 cycles at 1C rate.[16] Based on this bimodal concept, by fabricating ~300 nm carbon spheres instead of bulky carbon, more sulfur up to 70wt% can be incorporated while still having improved cycling performance.[17]

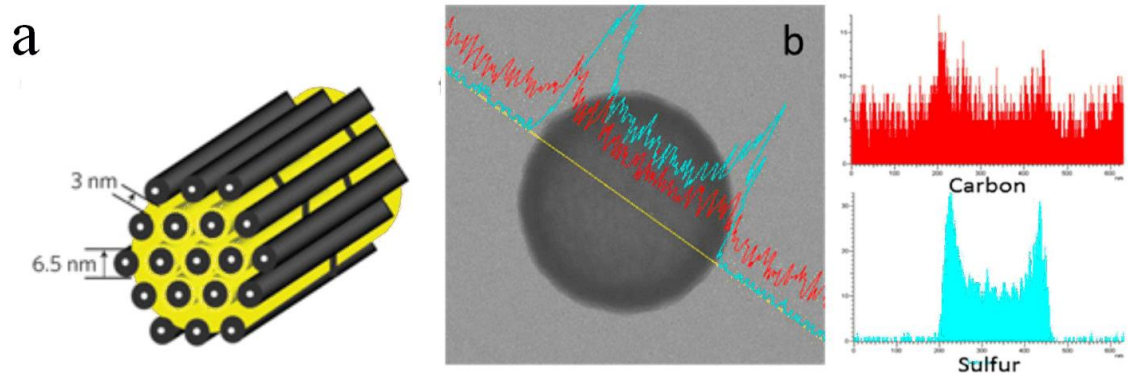

Figure 1.2 (a) The schematic illustration of CMK-3 carbon host (black) impregnated with sulfur (yellow). CMK-3 consists of hexagonally arranged and interconnected hollow carbon nanofibers (~ 6.5nm) which give rise to ~3 nm ordered pores, reproduced from reference 15. (b) Porous hollow carbon spheres (formed with surfactant pore former) with 70 wt% of sulfur infiltrated. A line scan over the sphere for carbon and sulfur elements reveals that sulfur exists not only on the shell but also inside the void space, reproduced from reference 19.

Hollow carbon sphere with porous wall is another field for porous carbon to impregnate sulfur. Archer *et al.* prepared hollow carbon spheres by pyrolysis of carbon precursor pitch that was coated on metal oxide nanoparticles template, followed by etching off the template.[18] The as-prepared carbon/sulfur composites exhibited a reversible capacity of 974 mA h/g with 91% retention over 100 cycles. It is claimed that sulfur could be impregnated into the interior void space and porous shells, but there is no direct evidence for that.[18] Recently, porous hollow spheres with controllable porosity were developed in our lab.[19] The carbon spheres with optimal porosity created either by polymeric pore former or KOH activation can confine sulfur in the carbon shell and inner

lining of the shell, as seen in **Figure 1.2b**. In addition to providing physical confinement on LiPSs, the void space also benefits accommodating volume expansion.

In addition to mesoporous carbon, microporous carbon with < 2nm pores is another option to confine sulfur. However, the electrochemistry is different. Gao *et al.* discovered a different voltage profile with only one plateau around 1.8 V when sulfur is confined in mircorpores. [20] A similar work was done by Guo *et al.* who proposed the sulfur molecular confined inside ~0.5 nm pore is actually small S_{2-4} molecular based on the observation that Raman peaks of cyclo-S_8 were absent in the carbon/sulfur composite and that the ~0.5 nm pore is not large enough to confine large S_8 molecular (>0.5 nm).[21] In this case, the transition from S_8 to soluble long-chain LiPSs is completely avoided and LiPS shuttle problem can be possibly even eliminated. Nonetheless, the disadvantage is that it is difficult to completely confine sulfur inside micropores and the sulfur remaining outside can still cause severe shuttle problem.

1.3.2 Graphene and its oxide

Graphene has the advantages of high electronic conductivity, high surface area and porosity and feasibility to tune the hydrophilicity/phobicity by surface functionalization. There are basically two ways to utilize graphene or its oxides in a sulfur cathode. The first approach is a core-shell structure by wrapping sulfur particles with graphene oxide nanosheets. The connection of hydrophobic sulfur particles and hydrophilic graphene sheets (with negative charge) is the major issue in order to achieve uniform and complete wrapping, for suppressing the LiPSs dissolution. To solve this problem, either non-ionic polymer cushion layer[22] or cationic surfactant[23] was used as a

linker. An interesting method of one-pot synthesis of graphene-wrapped sulfur where sodium polysulfide is oxidized with the presence of graphene oxide is more facile and effective in wrapping sulfur particles. [24]

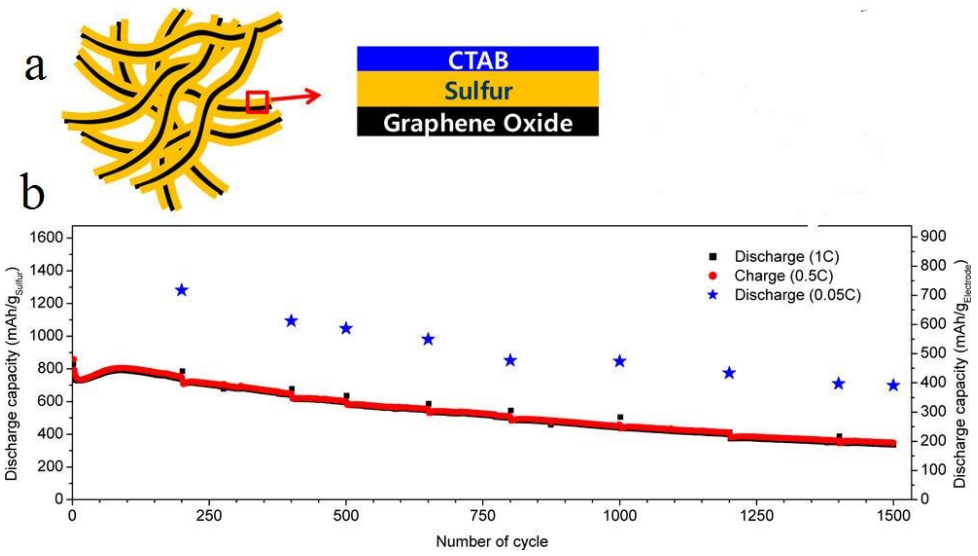

Figure 1.3 (a) A scheme demonstrating the sandwich layered structure of sulfur composite in reference 27. (b) The discharge and charge capacity retention over 1500 cycles for the composite shown in (a) with 80 wt% of sulfur. The star in blue represents the capacity of the cell upon periodical discharge at C/20. Reproduced from Reference 27.

Another approach is the utilization of graphene oxide as an anchor to immobilize sulfur that is *in situ* formed. [25-27] Zhang *et al.* was able to probe the interaction between oxygen groups on graphene oxide with sulfur through X-ray adsorption spectroscopy. [26] An *ab initio* calculation demonstrated the enhanced sulfur binding to graphene oxide sheet via epoxy and hydroxyl groups as well. After removing excess sulfur mass outside of graphene pores by thermal treatment, the cathode with 66 wt% of sulfur maintained 954 mA h/g after 50 cycles at C/10.[26] Recently, the same group reported a significant

improvement in battery performance using a multi-faceted approach, in which the amount of cationic surfactant cetyltrimethyl ammonium bromide (CTAB) was increased not only to connect sulfur and graphene oxide, but also to act as another layer to prevent the dissolution of surface LiPSs (**Figure 1.3**).[27] With modification in other aspects (binder, ionic liquid electrolyte and different charge rate than discharge), the composite with 80 wt% of sulfur was able to maintain 1500 cycles with a low decay rate of only 0.039% per cycle.[27] However, this improvement is attributed to a combination of multiple approaches and it is difficult to clarify which approach alone is the most effective.

1.3.3 Polymeric materials

The applications of polymeric materials on sulfur cathode can take advantages of physical confinement of LiPSs,[15,28] the interfacial interaction with LiPSs,[29, 30] chemical bond formation with elemental sulfur (vulcanization) or L_2S,[31-33] or combinations of them.

Our group was able to coat the aforementioned CMK-3/S composite with a hydrophilic polymer - polyethylene glycol (PEG), which further hindered the diffusion of LiPSs into electrolyte and thus improved the cycling performance.[15] This is due to both physical confinement and the adsorption of LiPSs by PEG via electrostatic forces between hydrophilic species. Another example of using polymer for physical confinement is wrapping commonly used graphene-oxide/sulfur composites with cross-linked amylopectin through intermolecular interactions. Compared with unwrapped ones, this composite exhibited much enhanced capacity retention over 100 cycles.[28]

Since LiPSs is hydrophilic, polymers with hydrophilic functional groups are expected to have strong interaction with LiPSs than hydrophobic carbon. Cui *et al.* has

coated the interior of hollow carbon fibers with amphiphilic polyvinylpyrrolidone (PVP) before infiltrating sulfur, which has alleviated the detachment of discharged product Li_2S from carbon support, confirmed by a comparison of transmission electron microscopy (TEM) images of electrode with and without coating (**Figure 1.4**).[29] This is probably due to the absorption of intermediate LiPSs rendered by hydrophilic pyrrolidone groups during cycling, evidenced from *ab initio* calculation.

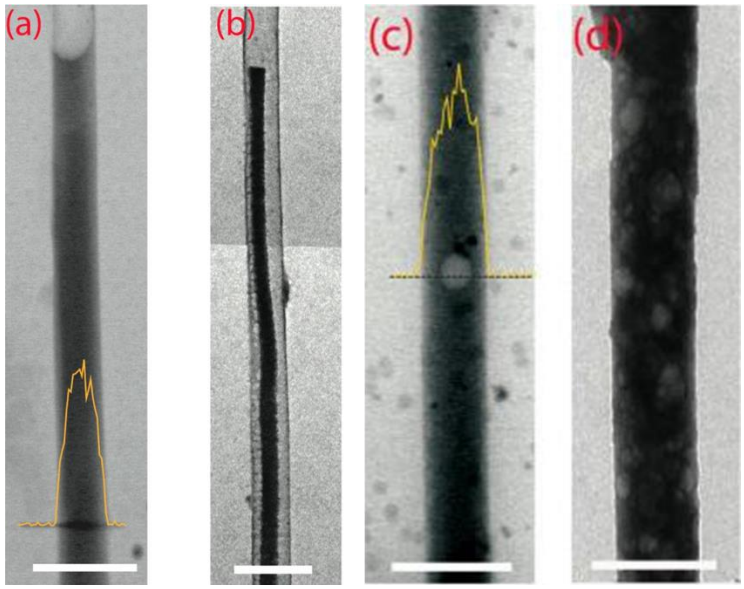

Figure 1.4 TEM images of the carbon fiber-sulfur composites without (a, b) and with (c, d) PVP modification, before discharge (a, c) and after first discharge (b, d). The yellow lines represent the sulfur distribution signal across the cross section lines. The comparison shows that with PVP modification, the discharge product (Li_2S, dark part) detachment from carbon walls was greatly alleviated. The scale bars are 500 nm in all images, reproduced from reference 29.

A further step forward in utilization of PVP was to directly encapsulate monodisperse hollow sulfur nanospheres. In addition to the absorption ability of PVP,

physical confinement further prevented LiPSs dissolution and the void space inside hollow sulfur paticles can mitigate volume expansion upon discharge.[30] Capacity decay was as low as 0.046% per cycle over 1000 cycles at C/2. However, sulfur cathode with a further coating of a poly(3,4-ethylenedioxythiophene) layer exhibited better cycling, probably because this layer is conductive to promote the electron penetration to the sulfur nanospheres, whereas PVP is not.

Introduction of sulfur by forming chemical bond with polymer support is another scope of efforts on anchoring sulfur/LiPSs. Liu *et al.* has used polyaniline (PANi) nanotubes to host sulfur. By reacting sulfur with PANi at 280 ^{o}C, part of the sulfur was incorporated into polymer backbone forming disulfide bonds, while the rest was still present in the interior pores of the nanotube in large fraction. Capacity increased by 80 mA h/g (compared with initial capacity) over 100 cycles, probably due to gradually enhanced electrolyte infiltration into porous structure over cycling. However, irreversible disulfide bonding formation upon charge can cause capacity loss.[34] A similar way to use PANi was performed by Abruña *et al.*, where PANi was coated on sulfur nanospheres and further heat treatment gave rise to not only chemical bonding but also void space inside the capsules after sulfur partial evaporating (**Figure 1.5a**). It was shown that after 5th cycle, the yolk-shell structure still remained undestroyed (**Figure 1.5 b, c**).[32] An interesting study on copolymerizing sulfur and vinyl monomers (termed inverse vulcanization) gained attention recently, because sulfur is completely bonded within the polymer network and this method is more facile and inexpensive. The composite with 90 wt% of sulfur retained 823 mA h/g after 100 cycles at C/10.[31] The electrochemical

mechanism needs further investigation, regarding how the sulfur bound to polymers evolve over discharge/charge.

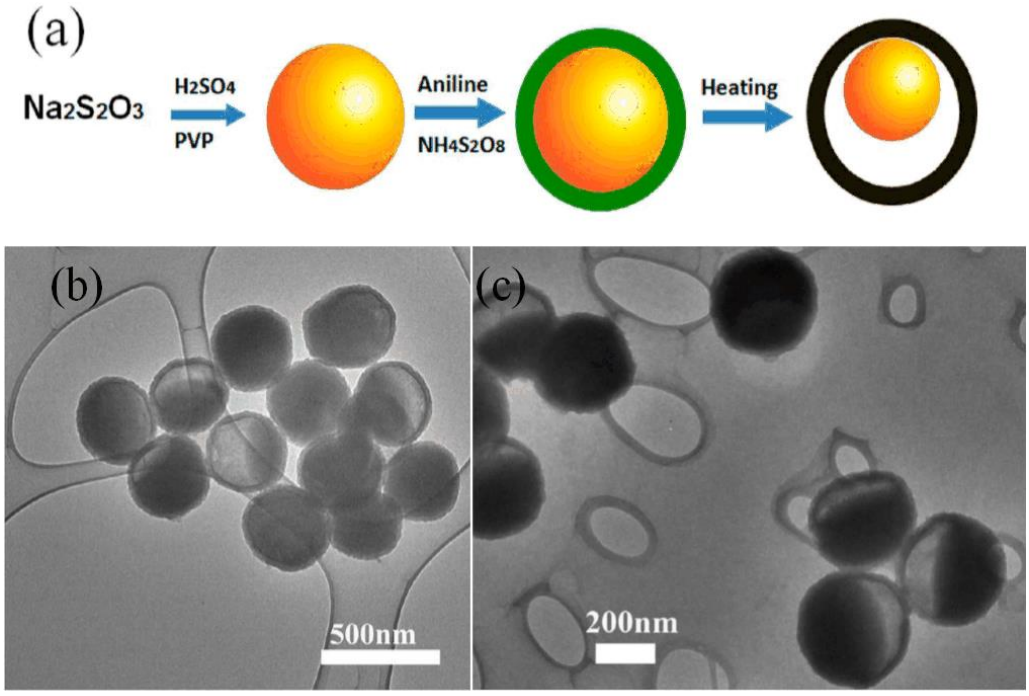

Figure 1.5 (a) Scheme showing the synthesis of PANi-S yolk-shell structure, with yellow, green and black parts representing sulfur, PANi and vulcanized PANi, respectively. (b,c) TEM images of the PANi-S yolk-shell structure before cycling (b) and after 5th charge (c), reproduced from reference 32.

1.3.4 Metal oxides

The use of metal oxides originated with mesoporous silica (SBA-15) as LiPS reservoir.[35] SBA-15 can adsorb LiPSs at the intermediate stage of discharge/charge through surface/ pore adsorption and relieve the LiPSs for further reduction/oxidation at the ending stage driven by concentration gradient. It was observed that during the intermediate stage, there was higher sulfur concentration on silica particles than carbon

hosts. A further understanding on the function of porous TiO_2 additives reveals that the LiPS adsorption is also related with chemical adsorption as demonstrated by Raman spectroscopy.[36] Nonetheless, there should be a compromise on the amount of additives used because too much of non-conductive additives can hurt the electronic conductivity and energy density of the whole electrode.

Another method on utilizing metal oxides is to coat on carbon/sulfur composite or sulfur particles.[37,38] Our group has successfully coated thin oxide layers (SiO_x and VO_x) on the acid-treated CMK-3/S composite and effectively suppressed LiPS dissolution. The hydroxyl groups on carbon initiated the growth of metal oxides. Another work involves a yolk-shell structure cathode where amorphous TiO_2 was coated on sulfur spheres at room temperature, followed by dissolving out part of sulfur to create void space.[37] Due to the confinement of the metal oxide layer, void space to accommodate sulfur expansion and short path for Li^+ ion transport, the composite experienced only 0.033% of capacity loss per cycle over 1000 cycles at C/2. However, the non-conductive TiO_2 layer can hurt the electron transfer across to sulfur particles, calling for more carbon additives in the electrode.

1.4 Current approaches on other aspects

In addition to trapping LiPSs within the cathode side, there are some approaches on other aspects to prevent LiPS shuttle problem and to extend cycle life, including using LiPS-insoluble electrolytes, interlayer between cathode and separator, modified separator as well as passivation of the anode.

1.4.1 Polysulfide-insoluble electrolytes

The problem of LiPS dissolution can be alleviated by using non-ether-based electrolytes, among which solid-state electrolytes and ionic liquids are mostly studied. For example, Li_2S-P_2S_5 system has been widely used as solid electrolytes with sulfur or Li_2S as cathode material, due to its relatively high ionic conductivity.[39] Although polysulfide shuttle can be possibly eliminated, it has problems, *e.g.* low ionic conductivity at room temperature, high electrode/electrolyte interfacial resistance, causing low rate capability and low sulfur utilization. On the other hand, room temperature ionic liquids (composed of entirely bulky ions) conjugated with lithium salts and solvated ionic liquids (*i.e.* equimolar mixture of lithium salts with glymes) can also suppress the dissolution of LiPSs. [40,41]

With the commonly used ether-based electrolyte, the dissolution can also be suppressed by increasing the concentration of solubilized lithium salts, based on the common ion effects. In the case where the lithium salt is concentrated enough to seize all sites for complex formation, there is no solubility for LiPSs any more, as lithium polysulfide is also a lithium salt. However, this can increase the viscosity of electrolyte and induce higher polarization. Another facile way is to properly adjust the amount of electrolyte used in cell to a minimized level to reduce the amount of LiPSs that can dissolve, while there is enough electrolyte for electrode infiltration.[42] This is not a universal approach for all cell systems though, because it depends on the cell design and cathode structures and components.[43]

1.4.2 Interlayers and separator modification

A unique design of placing a porous carbon membrane between cathode and separator was made by Manthiram *et al.* High surface area carbon black mixed with binder was used to make the microporous membrane. The interlayer can provide conductive support and also physically inhibit the LiPSs from diffusing onto anode side.[44] Regarding the separator, another interesting reserch by Huang *et al.* was conducted on coating the commonly used Celgard separator with Nafion solution to prepare an ionic selective membrane. In principle, the sulfonate groups SO_3^- on the ionic separator allow ion hopping of positive Li^+ over the pore channels, but reject hopping of negative S_n^{2-} anions.[45] The authors were able to demonstrate the effects of this electrostatic shield by the comparison that the electrolyte on anode side did not turn brown on cycling with this modified separator but it happened for unmodified separator. A low capacity decay rate of 0.08% per cycle was achieved over 500 cycles.

1.4.3 Anode protection

The problems with regard to lithium metal anode for Li-S battery include not only dendrite formation, but also its contribution in LiPS shuttle that causes insulating Li_2S on anode surface and low CE. The mostly widely used approach is adding $LiNO_3$ in electrolyte which can lead to the formation of a favorable surface layer on lithium metal anode. X-ray photoelectron spectroscopy (XPS) has shown that $LiNO_3$ in electrolyte is reduced to Li_xNO_y on lithium metal while in the presence of LiPS, Li_xSO_y is formed.[46] This means LiPS (or possibly Li_2S) is consumed on the passivation process. Ideally, once the passivation film forms, further LiPS reduction at anode side and shuttle phenomenon

could be inhibited. However, in fact the dynamic formation of dendrites keeps exposing fresh lithium surface and initiating new round of LiPS shuttle and then consumption of $LiNO_3$ until $LiNO_3$ is out. Therefore, this method cannot completely solve the problem. A similar effect was achieved by adding P_2S_5 in electrolyte. Ionic conductive Li_3PS_4 was found to be the dominant species on lithium anode surface as confirmed by Raman spectroscopy.[47]

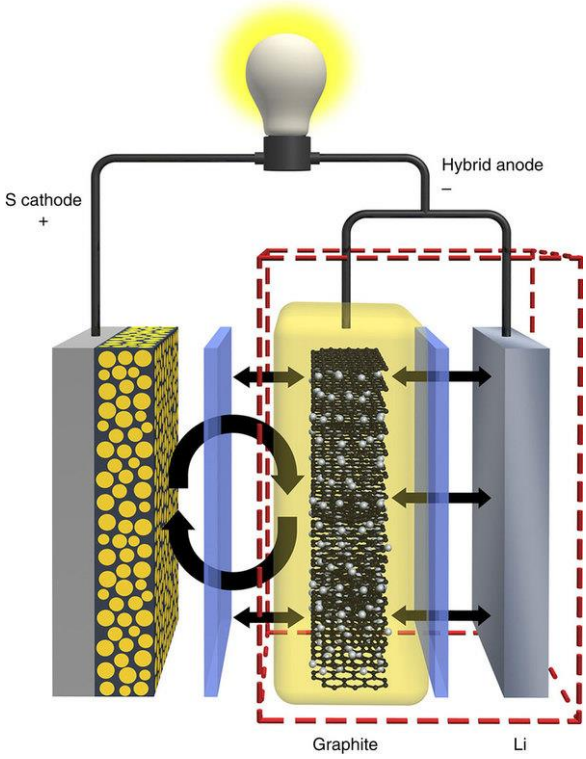

Figure 1.6 Scheme of the hybrid anode design, reproduced from reference 48.

Recently, Liu *et al.* designed a different anode structure to shift the interfacial redox reaction away from the metal surface by electrically connecting lithium metal with a graphite layer in the front as shown in **Figure 1.6**. Since graphite has slightly higher redox potential than lithium, graphite will remain lithiated and supply Li^+ ions on demand. On the other hand, lithiated graphite and lithium metal maintain pseudo-equal potential. It

was proposed that upon discharge, the dominant process is that graphite pumps Li^+ ions from lithium metal and relived them to the electrolyte. What benefits is that the parasite side reaction aforementioned will predominately occur on the graphite surface rather than the metal surface, alleviating the dynamic dendrite formation. Upon charge, the Li^+ ions preferentially plate on lithium metal. Therefore, the dynamic exposure of fresh lithium metal and polysulfide shuttle can be avoided. However, more investigation is needed to further understand why this works. [48]

1.5 Summary

Elemental sulfur was first introduced as a positive electrode material by Herbet and Ulam in 1962, [49] but its practical application has been hindered by the problem of LiPS shuttle. Since the introduction of mesoporous carbon as sulfur host, vast number of literatures have been reported on optimizing Li-S battery and indeed great progress has been made on increasing coulombic efficiency, extending cycling life and increase energy density. A good sulfur host material has to be both conductive and effective in suppressing LiPS diffusion. Among these efforts, most are devoted on using carbonaceous materials (*e.g.* porous carbon, graphene and polymeric materials) on the cathode side via physical confinement and/or chemical interactions. Metal oxides have also shown perspectives as sulfur host, but all of the ones studied are non-conductive. Despite these efforts, the LiPS diffusion and shuttle problem still remained to be further improved. This cannot be solely solved by looking at cathode side though. Innovations at the lithium metal anode or replacing lithium metal with other anode materials such as graphite and silicon with good cycling are also critical. Equally important, developing an

electrolyte system that is not only polysufide-insoluble but also highly Li^+ conductive is also a promising perspective.

1.6 Scope of this thesis

This thesis will be focused on new sulfur host materials to effectively suppress LiPS dissolution and enhance long-term cycle performance of Li-S cells. In ***chapter 1***, a general introduction on the demand for energy storage devices and pertinent researches that have been undertaken on Li-S batteries in the past. ***Chapter 2*** describes the characterization methods and techniques used in this thesis. ***Chapter 3*** examined a reduced titanium oxide as a sulfur host material and the improved electrochemical performances. ***Chapter 4*** introduced the synthesis of nanostructured MgB_2 working as a novel sulfur host material.

Chapter 2 Characterization methods and techniques

2.1 Materials characterization

2.1.1 X-ray diffraction

X-ray diffraction (XRD) has become the most commonly used technique to identify phase composition and analyze crystal structures. The development of XRD derives from three important discoveries: Wilhelm Röntgen discovered X-ray in 1985; Laue *et al.* discovered X-ray radiation can be diffracted by crystals in 1912; Sir William Bragg discovered the law to explain the appearance of a diffracted pattern through interference of X-ray reflected from the crystal planes, known as "Bragg's Law" (**equation 2.1**).

$$n\lambda = 2d\ \sin\theta \qquad (2.1)$$

Where θ represents the angle between incident X-ray beam and the parallel planes and d represents crystallographic planes under probe, as shown in **Figure 2.1**. When parallel X-ray beams are diffracted by neighboring parallel atomic planes that maintain a distance of d with each other, the beam going into a deeper plane travels an extra distance of $2d \sin\theta$. In the case where Bragg's law is satisfied, meaning $2d \sin\theta$ is a multiple (n) of the wavelength (λ) of incident beam, the two parallel beams will be in phase after being diffracted back. There will be a diffracted pattern (observable intensity of reflected X-ray) in this case. Therefore, with this θ known, d will be calculated and assigned to one plane index.A series of the θ detected will give a whole pattern giving all plane indices.

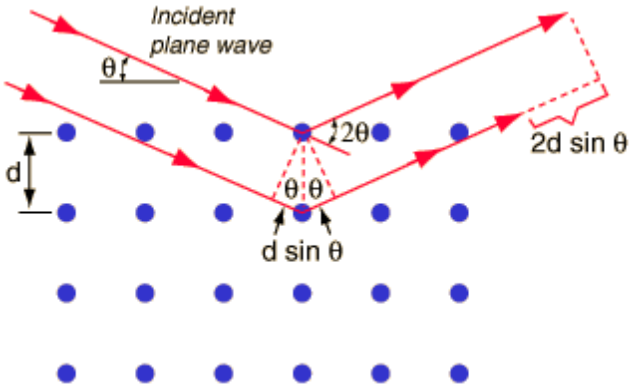

Figure 2.1 Schematic illustration of Bragg's law, reproduced from reference[50].

Bragg's law is applicable to powder XRD because when an X-ray beam hits a finely ground sample containing plenty of small crystals, there must be a fraction of crystals that has crystallographic planes orientated with one Bragg angle for the diffraction to occur and this angle θ corresponds to a plane index. When rotating the sample stage with regarding to incident beam, a pattern containing all characteristic diffractions can be recorded. XRD patterns are unique for compounds in terms of structures and components. With the help of a comprehensive database, the component along with crystal structure of a sample can be determined. Therefore, what an X-ray diffractometer does is to scan the sample over a range of θ (or 2θ) and to measure the intensity of diffracted X-ray as a function of the angle. Any plane that possibly diffracts X-ray will be detected. The overall area under all peaks belonging to one phase on the XRD pattern is proportional to the weight fraction of this phase in the sample powder.

With regard to nanocrystalline samples (usually < 1 μm), the peaks broaden due to the diffraction by the grain boundaries. The relation of domain size (coherence length, L) and full width at half maximum intensity (β) can be described by Scherrer equation as in **equation 2.2**.

$$L = \alpha \lambda / (\beta \cos \theta) \quad (2.2)$$

XRD patterns in this thesis were collected on Bruker D8-Advance powder X-ray diffractometer operating at 40 kV and 30 mA and using Cu-Kα radiation (λ=0.15405 nm). Samples were put on a zero-background silicon holder and air-sensitive samples were protected in a chamber with Kapton film window.

2.1.2 Scanning electron microscopy and energy dispersive X-ray spectroscopy

Scanning electron microscopy (SEM) is an important tool to directly look at the morphology and topography of micro/nanostructures of a solid sample. In an SEM instrument, the electron with high energy (up to 40 keV) hits the solid surface, generating secondary electrons, back-scattered electrons, transmitted electrons, and characteristic X-rays (fluorescence) from the cross-section area of the sample. They are probed by corresponding detectors. The density of electrons contains information on the morphology of the surface and some signals can be translated into high resolution images. Secondary electron mode can provide more information on the topography while back-scattered electrons are more informative on element distribution. When secondary electron is generated, a shell electron with relatively low binding energy is excited leaving a hole behind. Then one electron from outer shell has to jump into the hole to remain lowest energy possible, during which the excessive energy is relieved by emitting X-rays. This is used for identifying element for energy dispersive X-ray spectroscopy (EDX). As a semi-qualitative technique, EDX elemental mapping can provide information on the distribution of each element over the area projected.

SEM imaging and EDX measurements in this thesis were carried out either on a Zeiss LEO 1530 field or Zeiss Ultra Plus field emission SEM. Secondary electron mode was used when taking images. Nonconductive samples were coated with gold before imaging.

2.1.3 Transmission electron microscopy

Transmission electron microscopy (TEM) utilizes electrons with even higher energy (200 keV) and shorter wavelength (λ = 0.025Å) that is comparable with atom diameter, so TEM images can have much higher resolution than SEM. TEM samples were imaged on JEOL 2010F TEM/STEM operating at 200KeV for this thesis. In a scanning transmission electron microscope (STEM), the image is generated by scanning the focused beam over a sample that is usually ultra-thin slice. Samples were dispersed onto a copper grid before imaging. Both dark-field and bright-field imaging were used in this thesis. In dark-field imaging higher atomic number elements appear brighter in the image and low atomic number elements appear darker and *vice versa* for bright-field imaging.

2.1.4 Surface area/ pore size characterization

Surface area, pore volume and pore size distribution (PSD) were determined on a Quantachrome Autosorb-1 instrument. Samples were degassed at 180 ^{o}C on a vacuum line before measurement, except for sulfur containing samples, degassing at 50 ^{o}C was used to prevent the vaporization of sulfur. Nitrogen adsorption/desorption isotherms were collected at 77 K in liquid nitrogen bath. A N_2 adsorption isotherm is the plot of volume of nitrogen adsorbed on the surface of sample as a function of the relative pressure in the

sample chamber. It can provide information on the surface area and type of pore size. During the measurement, the sample is loaded into a quartz tube and evacuated first. Nitrogen gas is periodically introduced into the sample tube and adsorbed on the surface of the sample at desired pressures. The amount of N_2 adsorbed can be obtained by comparison to the balance tube. In this thesis, the surface area was determined from Brunauer-Emmett-Teller (BET) method from multi-point analysis and the total pore volume was calculated from the volume of nitrogen adsorbed at a relative pressure (P/Po) of 0.99. The PSD was calculated using the quenched solid state functional theory (QSDFT) method.

2.1.5 Thermal gravimetric analysis

Thermal gravimetric analysis (TGA) was performed under constant nitrogen flow on a TA Instruments (SDT Q600 analyzer). TGA, combined with differential scanning calorimetry (DSC) is usually used to study the thermal properties and components of a sample. By increasing the temperature in a linear way, the mass change and thermal flow from sample (calculated by comparison with the reference) can be recorded. The thermal decomposition temperatures, component information and phase transformation can thus be obtained. In this thesis a standard temperature program of 10 ℃/min ramp was used. The weight percentage of sulfur was determined by the weight loss between 200-400 ^{o}C.

2.1.6 X-ray photoelectron spectroscopy

XPS, also known as electron spectroscopy for chemical analysis, is based on the photoelectric effect described by Einstein. Photoelectrons are electrons that are emitted from the ground state atoms upon photon radiation, which is X-ray in this case. When an

atom receives energy from X-ray, it gets excited from ground state, during which core electrons are emitted into vacuum. The energy transfer during this process can be described as **equation 2.3**.

$$E_{binding} = \mathrm{hv} - E_{kinetic} - \phi \qquad (\mathbf{2.3})$$

Where $E_{binding}$ represents the binding energy of the electron ejected in its ground state, $E_{kinetic}$ represents the kinetic energy of the photoelectron after emission, hv represents the energy of X-ray that has been adsorbed, and ϕ is the work function of the spectrometer, irrelative to the sample. The spectrometer probes the kinetic energy and the number (intensity) of photoelectrons, so with the hv known for an X-ray, the binding energy can be calculated. XPS must be carried out in ultra-high vacuum in order to avoid the interference from gas phase collisions with photoelectrons. Using x-ray with a high enough energy, in principle, a spectrum of the intensities of all electrons emitted (photoelectrons and Auger electrons) as a function of binding energy (eV) can be obtained. Each element has its characteristic peaks, except hydrogen and helium. More importantly, XPS is unique to provide chemical state information of an element, because binding energy of the electrons emitted can be shifted because of a change in the chemical shift. Therefore, high resolution XPS specified on each element can provide information on the chemical environment around one atom.

XPS analysis in this thesis was performed by using a multi-technique ultra-high vacuum Imaging XPS Microprobe system (Thermo VG Scientific ESCALab 250) equipped with a hemispherical analyser (of 150 mm mean radius). Data were collected with pass energy of 20 eV for the core-shell spectra, with the takeoff angle (defined as

the angle between the substrate normal and the detector) fixed at 0 degree. For conductive samples, a monochromatic Al Kα (1486.6 eV) 150 W X-ray source with 0.5 mm circular spot size was used, whereas for non-conductive samples, non-monochromatic Al Kα X-ray source from twin anode was used. The sample was transported to the XPS chamber under Ar, and transferred into chamber very quickly, in order to protect from air contamination.

2.1.7 Electronic conductivity measurement

Electronic conductivity of the powder samples synthesized in this thesis was measured on a Jandel four-point probes connected with RM3000 test unit. The four-point probe technique uses two separate pairs of electrodes, *i.e.* current-carrying and voltage-sensing eletrodes. The two outer current-carrying electrodes force a current flow over the resistance to be measured and the two inner voltage-sensing electrodes sense the exact voltage drop on the resistance. Its advantage over conventional two-point probe is based on the fact the additional voltage-sensing electrodes exclude the voltage drop from the measuring wires.

To measure the bulk conductivity of the powder samples, samples were pressed to pellets which were then sintered at 800 ^{o}C under Ar to promote the sintering between particles. The Jandel instrument provides the sheet resistance R_s in ohm per square (Ω cm^{-2}) and the thickness s (cm) is measured by micrometer, so the bulk conductivity σ (S cm^{-1}) can be given as in **equation 2.4**:

$$\sigma = \frac{1}{R_s\, s} \qquad \textbf{(2.4)}$$

2.2 Electrochemical techniques

2.2.1 Coin cell configuration

In this thesis, 2325 type coin cells were used to look into the electrochemical performance of the electrode materials. A coin cell configuration is shown in **Figure 2.2**. The cathode was made by mixing the active material composite, conductive carbon additive and polymer binder in a solvent to form a slurry and then slurry-casting or drop-casting onto carbon-coated aluminum foil or carbon paper collector (P50, Avcarbon). The electrode was then dried at 60 ^{o}C overnight to vaporize the solvent. The cell was assembled inside Ar-filled glovebox. The electrolyte consists of a lithium salt dissolved in a mixture of ether-based solvents, with the presence of certain concentration of lithium nitrate for the protection of lithium metal anode.

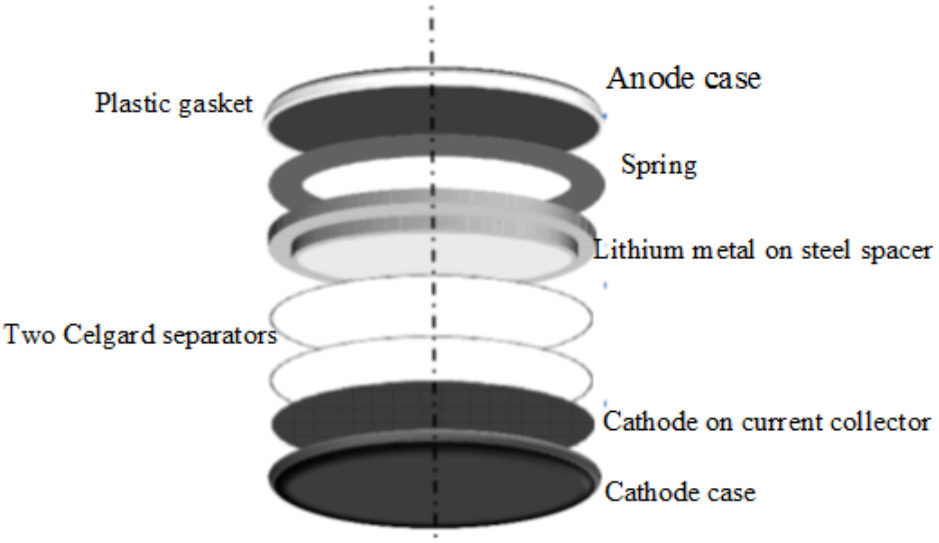

Figure 2.2 Configuration of a coin cell used in this thesis. [51]

2.2.2 Galvanostatic cycling

This mode of electrochemical measurement is the most standard and commonly used technique to characterize capacity and cycle life. In this mode, a constant current is applied to the cell upon discharge/charge and inverted at the cut-off voltage. Within each discharge/charge cycles, the voltage of the cell is recorded as a function of step time or capacity delivered and the overall capacity corresponds to the point reaching cut-off voltage. Generally, a linear dependence of voltage on capacity (a slope in the voltage profile) corresponds to a solid-solution single-phase reaction whereas a plateau of potential irrespective to capacity corresponds to a two-phase reaction. Long-term cycling performance can be described by a plot of specific capacity retained as a function of cycle numbers. Rate capability of a cell can be evaluated by increasing the current periodically over certain number of cycles and then returning to the original rate. Minimum capacity change is desired for high rate capability and powder density. The galvanostatic cycling was carried out using a BT2000 battery cycler (Arbin Instruments).

2.2.3 Cyclic voltammetry

In the cyclic voltammetry (CV) measurement, the current of the cell is recorded as a function of the voltage applied which changes in a systematic manner- linear increase or decrease with time in the voltage window. Cyclic means the reversed trend of voltage when the potential gets to the limit. Upon increase of voltage, oxidation reaction occurs around certain voltage while reduction reaction occurs *vice versa*. The voltage applied can be considered as the pressure of electrons that can force the reactive materials to gain or lose electron, so this technique, compared with galvanostatic cycling, provide more

clear information at what voltage the redox reactions happen. By looking at the peak areas under certain peak in CV plot, the amount of materials involved in the reaction can be evaluated and the width of the peak - indicator of electrochemical response - either reflects the kinetics or some electrode/electrolyte interfacial effects. CV measurements in this thesis were carried out on a VMP3 potentiostat/galvanostat station with EIS/Z capabilities (Bio-Logic Science Instruments).

2.2.4 Electrochemical impedance spectroscopy

Impedance is a measure of the ability of a circuit to resist the flow of electrical current. In an electrochemical impedance spectroscopy (EIS) analysis, a small alternating current (AC) voltage is applied to an electrochemical cell and the current response is measured at open-circuit voltage. Because an electrochemical cell is a non-linear electric element, meaning the current response with regard to voltage is not linear (as seen in CV plots), a small amplitude of the voltage is necessary (1-10 mV) in order to make the process pseudo-linear. The AC voltage is usually applied as a sinusoidal excitation over a frequency range and the AC current response is analyzed as a sum of sinusoidal functions. In this case, the impedance can be described by a complex value consisting a real part and imaginary part at each frequency measured. Fourier transformation is used to transfer signals from time domain to frequency domain.

Nyquist plot used in this thesis is plotted with imaginary part of the resistance on y-axis and real part on x-axis. Generally, for an electrochemical cell, Nyquist plot consists of a series of semicircles (at high-frequency range on the left) related to resistance and capacitance within electrodes and on the electrode/electrolyte interface and

an inclined line (at low-frequency range on the right) related to electrolyte resistance. In this thesis, EIS measurements on two-electrode Li-S cells were carried out on VMP3 potentiostat/galvanostat station with EIS/Z capabilities (Bio-Logic Science Instruments). The DC voltage was kept at open-circuit voltage and the AC voltage of 5 mV in amplitude was applied with a frequency of 200 kHz-20 mHz.

Chapter 3 High-surface-area reduced titanium oxide with metallic conductivity as a sulfur host material

3.1 Introduction

As mentioned in **chapter 1**, the main problems concerning cathode design in Li-S battery lie in increasing the electronic conductivity and suppressing polysulfide dissolution and diffusion into electrolyte. Currently, most of researches were focused on carbonaceous materials (*e.g.* mesoporous carbons,[15] hollow porous carbon spheres,[19] graphene,[22,24,52] carbon interlayers[44]), taking the advantage of high conductivity and physical confinement effect from deliberate design on porous architectures. However, over long-term cycling, the LiPSs with a hydrophilic nature can still diffuse out of the open pores created by hydrophobic materials. The lack of chemical interaction has driven researchers for modifications on the carbonaceous materials, including creating oxygen functional groups[25,26] and CTAB[27] on graphene and amphiphilic modification[29] of carbon surface to anchor LiPSs. This has enabled improved control over LiPS dissolution indeed. However, these modifications actually lower the electronic conductivity of carbon host, which has compromised the original purpose of using carbon, that is, its high conductivity. In another word, maximum amount of oxygen groups on carbons are desired to trap LiPS on one hand, but on the other hand, more groups hurt the conductivity. Therefore, this contradiction can deteriorate the effectiveness of carbon. In addition to carbonaceous materials, metal oxides, either used as LiPSs adsorbents[35,36] or coating agent,[37,38,53] also demonstrated promise in solving the problems. Especially, the use of TiO_2 to coat sulfur nanospheres has enabled the cell to retain good capacity over

1000 cycles.[37] However, the fact that such superior performance was achieved with a low loading of sulfur in each electrode (0.4–0.6 mg_{sufur}/ cm^2) indicates the low kinetics of the electrode, due to non-conductive nature of TO_2. The TiO_2 coating might also hinder the electrolyte access to internal sulfur.

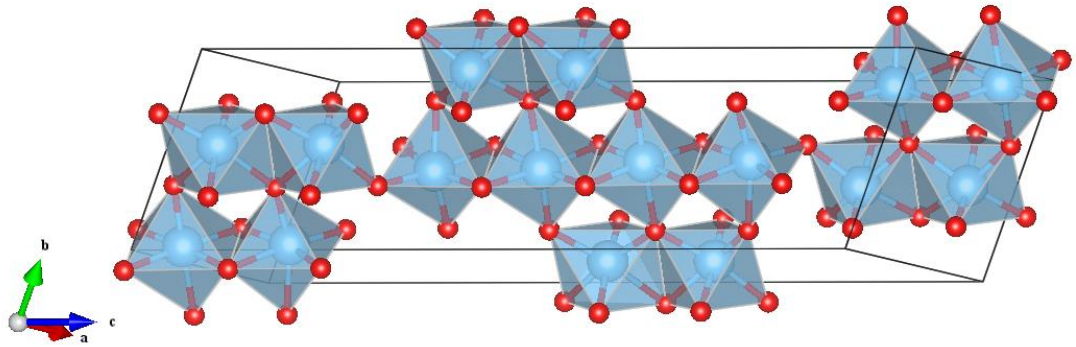

Figure 3.1 A representative unit cell of Ti_4O_7 showing its crystal structure, consisting of either corner- or edge-shared TiO_6 octahedra (small red spheres = O, large grey spheres = Ti).

These considerations have led us to develop a bifunctional sulfur host material that is not only highly conductive but which can also chemically bind LiPSs. Metal oxides which contain polar O-M-O units and are conductive can fulfill these roles. In this chapter, Ti_4O_7, a reduced form of titanium oxide, was synthesized in the form of high surface area and mesoporous, and tested as a sulfur host material for Li-S battery. Ti_4O_7 is a member of the Ti_nO_{2n-1} Magnéli phases, which are substoichiometric compositions of metallic titanium oxides that form a homologous series between TiO_2 and Ti_2O_3. Its structure is characterized by two-dimensional shear-plane slabs of Ti-O octahedra as shown in **Figure 3.1**. Ti_4O_7 has high bulk electronic conductivity as high as 2×10^3 S cm^{-1} at 298 K, [54] about 3-fold greater than graphite. This systematic approach to cathode

design results in very low capacity fade rate for composites containing up to 70 wt% of sulfur. In addition, the presence of strong metal oxide-polysulfide interactions is demonstrated by XPS analysis and LiPS adsorption studies. It is acknowledged that in this chapter, the mesoporous Ti_4O_7 was synthesized by Dr. Dipan Kundu from our lab and originally developed as a cathode material for Li-air cell. Dr. Marine Cuisinier and Brain Adam's discussions are also acknowledged.

3.2 Experimental

3.2.1 Synthesis of Ti_4O_7 and Ti_4O_7-S composites

Ti_4O_7 has been utilized as a Pt catalyst support for fuel cells, [55] but it has not yet been reported in a high surface area form, which is essential for sulfur encapsulation. A mesoporous Ti_4O_7 was synthesized via a polymer-mediated method, followed by post heat-treatment under an inert gas flow. This method relies on the cross-linking of titanium ethoxide with polyethylene glycol to form a gel that undergoes carbothermal reduction at high temperature and crystallizes.

In a typical synthesis, titanium (IV) ethoxide and PEG (M_n = ~400 g mol^{-1}) were mixed in a desired weight ratio followed by addition of ethanol to control the viscosity, which was then stirred at 80 ℃ for overnight, forming an amber yellow gel. The resultant gel was further dried at 100 ℃ for 6 h and then fired at 1000 ℃ under N_2 stream for 4 h with a heating ramp of 5 ℃/min. A possible reaction scheme is presented in **Figure 3.2**.

The sulfur composites were prepared via a well-established melt-diffusion method. Sulfur and Ti_4O_7 were mixed by grinding at desired ratios (60 or 70 wt% of sulfur in

composites) thoroughly and then pressed in a die which was then heated at 155 ^{o}C overnight. Heated pellets were well ground for electrode making.

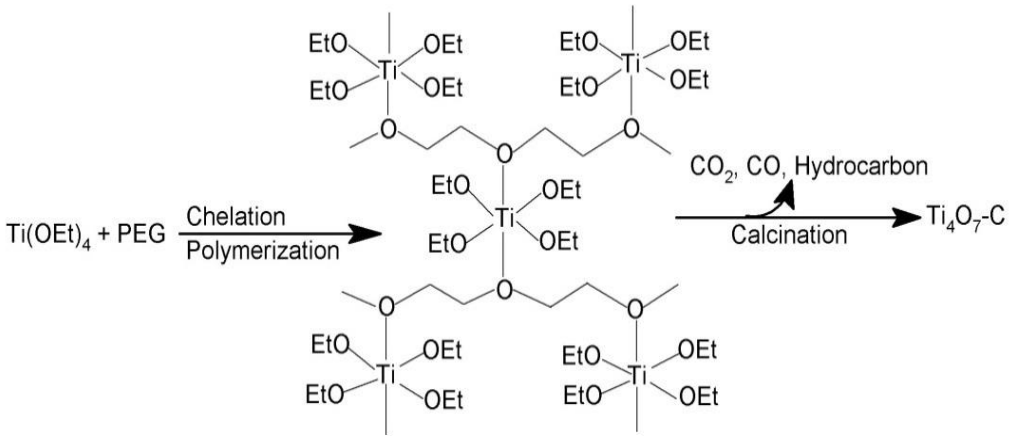

Figure 3.2 The synthesis process showing the polymerization of titanium ethoxides by chelating with PEG to form a network.

3.2.2 Electrochemical Measurements

Positive electrodes were constructed from Ti_4O_7/S-X (X=60 or 70, corresponding to the weight percent of sulfur), super P and polyvinylidene fluoride binder (PVDF) binder with a mass ratio of 8:1:1. The mixture was well dispersed in dimethylformamide (DMF) to form a thin slurry which was drop-cast onto a carbon paper (AvCarb P50) to fabricate the positive electrodes. Cells were assembled inside the glovebox with lithium foil as anode and an electrolyte of 1 M bis(trifluoromethanesulfonyl)imide lithium (LiTFSI) and 2 wt % of $LiNO_3$ in a mixed solvent of DME and DOL (v/v = 1:1). The cells were galvanostatically discharged/charged in the voltage window of 1.8-3.0 V at various C rates, except that 1.9-3.0 V was used for cycling at C/20 and 1.7-3.0 V for 2C. For EIS measurements, the DC voltage was kept at open-circuit voltage and an AC

voltage of 5 mV in amplitude was applied with a frequency range of 200 kHz-20 mHz. Nyquist plots of cells after certain numbers of cycle were obtained after galvanostatic discharge/charge at C/2. For CV measurements, a sweep rate of 0.1 mV/s within the 1.8 - 3.0 V window was applied.

3.3 Results and discussion

3.3.1 Physical characterization of Ti_4O_7 and Ti_4O_7 -S composites

XRD pattern of the as-synthesized Ti_4O_7 along with standard pattern from ICDD #500780 is shown in **Figure 3.3a**. XRD proves Ti_4O_7 is the primary crystalline phase formed. Elemental microanalysis indicates the inclusion of 15.4 wt% residual amorphous carbon from polymer decomposition. This is important both as an agent to maintain high surface area, and to serve as a hydrophobic component for binding elemental sulfur.

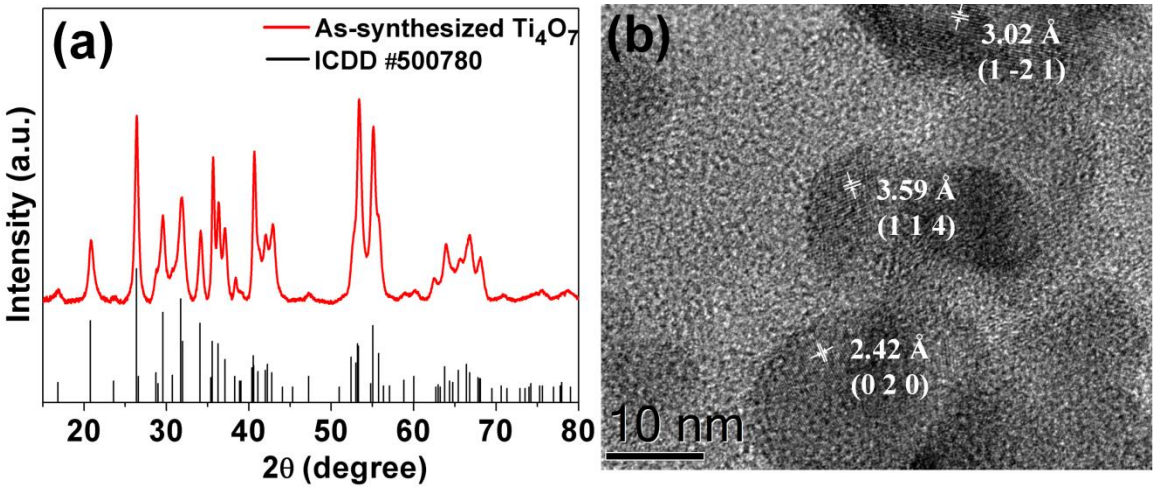

Figure 3.3 (a) XRD pattern of synthesized Ti_4O_7 along with peak characteristics of ICDD # 500780 reference; (b) High-resolution TEM image of synthesized Ti_4O_7 materials, with the crystal lattices indexed based on interplanar distances.

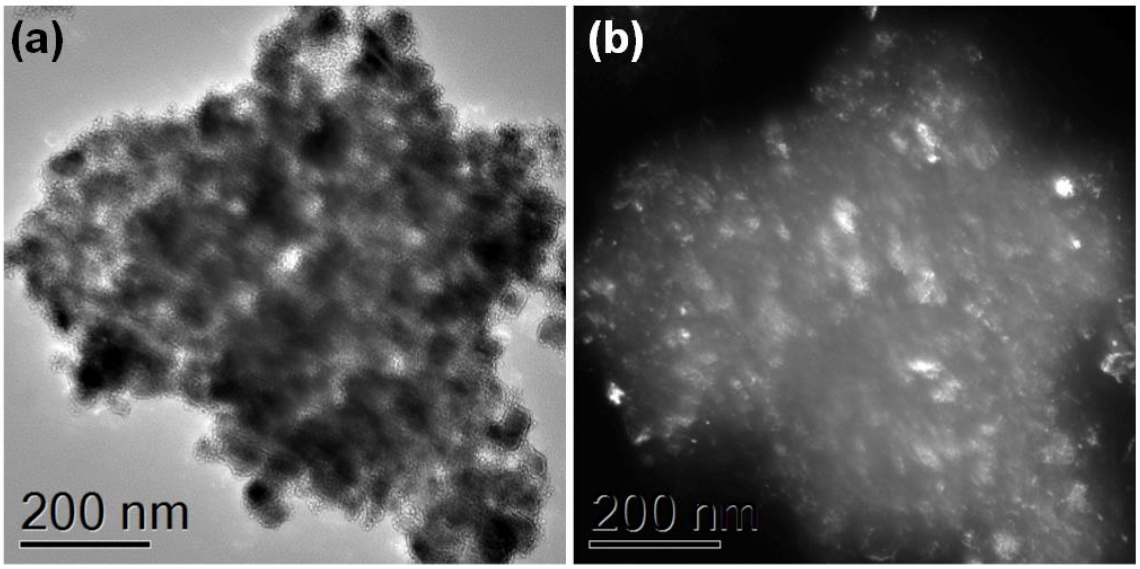

Figure 3.4 (a) Bright-field and (b) dark-field TEM images of synthesized Ti_4O_7, in identical region.

High-resolution TEM images (**Figure 3.3b**) further confirmed its crystalline structure, based on the indexed crystal planes via comparison with crystallographic parameters from ICDD #500780. **Figure 3.3b** also reveals the material is primarily comprised of ~8-20 nm particles of Ti_4O_7. Combined with the bright- and dark-field TEM images in **Figure 3.4**, it can be concluded that the Ti_4O_7 crystals (bright spot in **Figure 3.4b**) are dispersed in amorphous carbon (grey part in **Figure 3.4b**). This gives rise to a bulk electronic conductivity of 3.1 ± 0.1 S cm^{-1}, as measured by 4-point probe method.

The material exhibits a very high surface area and pore volume of 290 m^2 g^{-1} and 0.49 cc g^{-1}, respectively, based on N_2 adsorption/desorption measurements, as seen in **Figure 3.5a**. The PSD calculation in **Figure 3.5b** shows pores of ~1.5 nm and ~5-6 nm, confirming the presence of both micropores and mesopores. The high pore volume arises mainly from inter-particle mesopores, vital for effective sulfur impregnation. The

effective impregnation of sulfur into Ti_4O_7 host was determined by TGA analysis as seen in **Figure 3.6**. The weight loss at around 250-300 ^oC is due to the evaporation of sulfur. The weight percentages of sulfur in Ti_4O_7/S-60 and Ti_4O_7/S-70 were confirmed to be 60 wt% and 70 wt%, respectively. After impregnating sulfur, the surface area and pore volume decreased. Taking Ti_4O_7 /S-60 as an example, it has a much lower surface area of 3.39 m^2 g^{-1} and a pore volume of 0.02 cc g^{-1}, indicative of partial pore filling (**Figure 3.5 a and b**). The pore volume left is important for electrolyte infiltration into the interior part of the electrode.

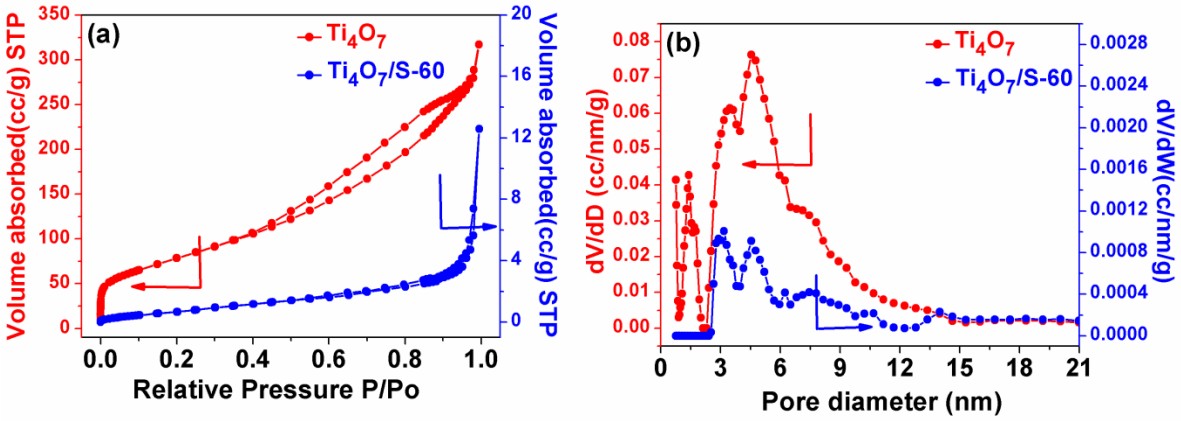

Figure 3.5 (a) N_2 adsorption/desorption isothermals of Ti_4O_7 and Ti_4O_7/S-60. (b) Pore size distribution of Ti_4O_7 and Ti_4O_7/S-60 calculated by QSDFT method.

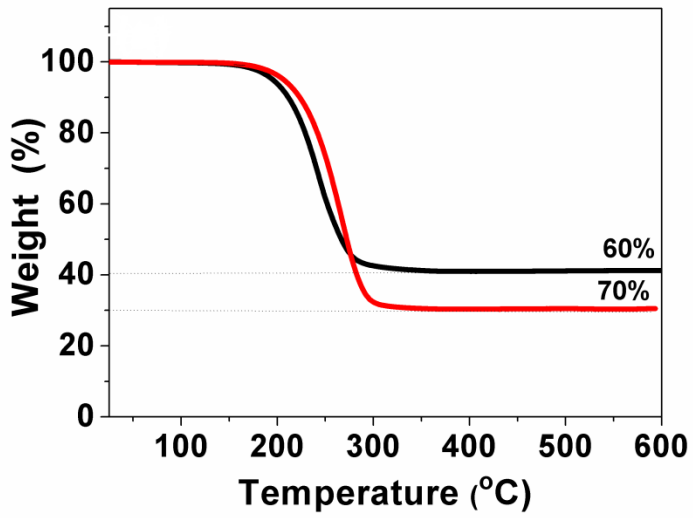

Figure 3.6 TGA curves of Ti_4O_7 /S-60 and Ti_4O_7 /S-70.

A further investigation into the distribution of sulfur was carried out on SEM imaging along with EDX elemental mapping. A representative SEM image of the composites shows a homogeneous, smooth conformal sulfur coating exists on the titania nanoparticles (**Figure 3.7**), and reveals no evidence for large sulfur masses. EDX elemental mapping over a larger area further confirmed the uniform distribution of Ti, O and S (**Figure 3.8**).

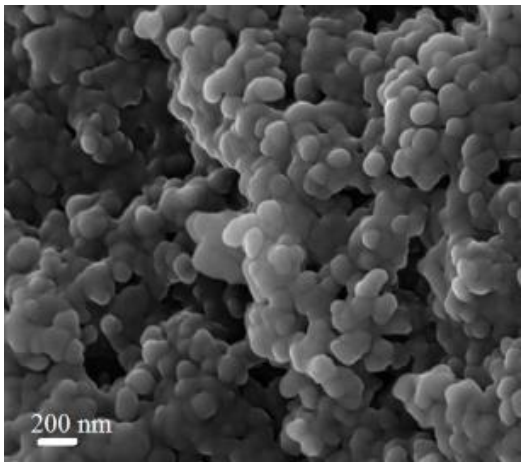

Figure 3.7 An SEM image of Ti_4O_7/S-60 showing absence of large sulfur mass.

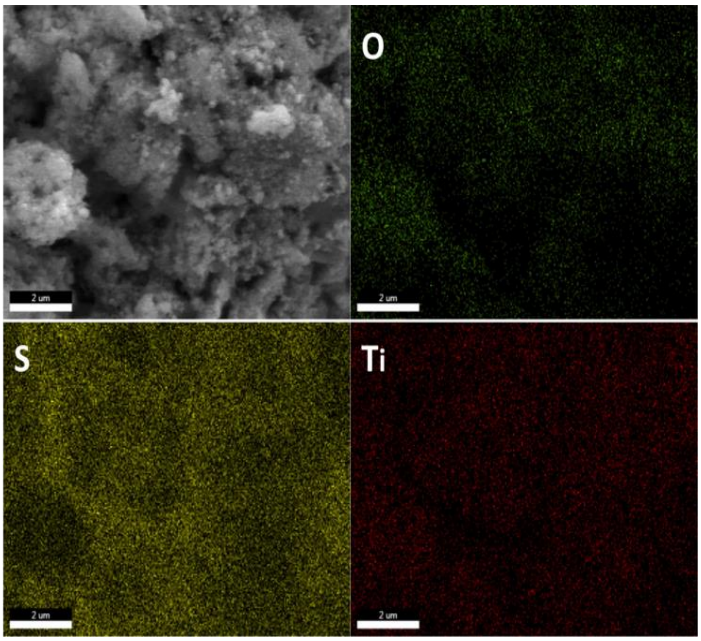

Figure 3.8 An SEM image of Ti_4O_7/S-60 composite and EDX elemental mappings of Ti, S and O in the corresponding area.

3.3.2 Ti_4O_7-LiPS interaction studies

3.3.2.1 Synthesis of lithium and sodium polysulfides

Li_2S_4 with a medium chain-length was used as a representative LiPS to study the Ti_4O_7-LiPS interaction. Solid state Li_2S_4 was synthesized by reacting elemental sulfur and lithium superhydride ($LiEt_3BH$) with desired ratio in anhydrous tetrahydrofuran (THF) for one hour inside the glovebox. Excess THF solvent was removed by applying vacuum under room temperature and the precipitates were retrieved by washing with THF, followed by vacuum drying, as reported previously.[10] Na_2S_2 and Na_2S_4 as proof references were prepared by reacting sodium sulfide nonahydrate with elemental sulfur with desired ratios in absolute ethanol under N_2 flow. The mixture solution was stirred under reflux for one hour and then cooled down to room temperature for overnight. The

solvent was removed by applying vacuum and the sample was further dried at 80 ^{o}C for 2 hours. It is acknowledged that the synthesis of sodium polysulfides were carried out by Dr. Marine Cuisinier.

3.3.2.2 Ti_4O_7-LiPS interaction

To confirm the idea of using metal oxide to adsorb and trap LiPSs in Li-S cell, the interactions of different cathode host materials (Ti_4O_7; carbon materials as comparisons) with Li_2S_4 were probed using XPS and visual discrimination.

To prepare the samples for XPS analysis, three Li_2S_4 solutions were prepared by dissolving 4 mg of Li_2S_4 in 5 mL of THF in each case. Then graphite (Alfa Aesar), VULCAN® XC72 carbon (Cabot Corporation) and mesoporous Ti_4O_7 were added to each solution. The mass added was adjusted so the total surface areas of the solids based on BET measurements were the same (5.8 m^2) in each case. For example, for Ti_4O_7 with a surface area of 290 m^2/g, 20 mg were added. To inspect the solution color, in the first step, immediately upon stirring, the suspensions were allowed to settle for a few minutes. For the second step, the solutions were further stirred for 1 h. All procedures were completed in the glovebox.

Demonstration of the superior intrinsic capability of Ti_4O_7 to bind Li_2S_4 was obvious, as shown in **Figure 3.9a,b**. Addition of Ti_4O_7 rendered the Li_2S_4 solution light yellow immediately upon contact and almost completely colorless after it was stirred for 1h - indicating strong adsorption - whereas the graphite or VC solutions remained intense yellow-gold, indicative of no interaction.

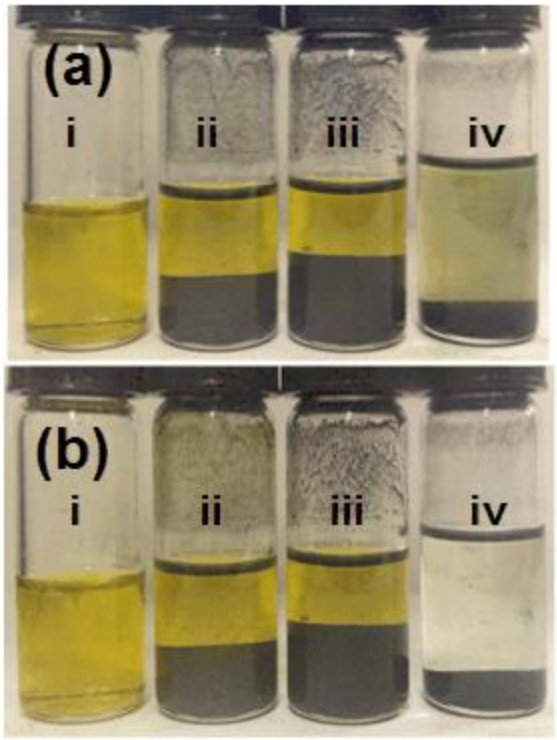

Figure 3.9 Sealed vials of a Li_2S_4/THF solution (i), and after contact with graphite (ii), VC carbon (iii) and Ti_4O_7 (iv), immediately upon contact (a) and after one hour stirring (b).

The materials were analyzed by XPS after centrifugation and vacuum drying and the S 2p spectra are shown in **Figure 3.10**. Only the peak position of the lower energy component of the $2p_{3/2}/2p_{1/2}$ doublet is listed, following convention. The spectrum of Li_2S_4 (**Figure 3.10a**) shows a 1:1 ratio of two contributions at 161.6 eV and 163.1 eV, ascribed to the terminal (S_T^{-1}) and bridging sulfur (S_B^0), respectively. This assignment is based on comparison of binding energies with those reported for copper polysulfides[56] and the similarity of the spectrum to that of sodium polysulfides we synthesized (**Figure 3.12a, b**). It is in full accord with the proposed chain-like structure of most LiPSs where

density functional theory (DFT) calculations show that the negative charge is localized at the termini.[25]

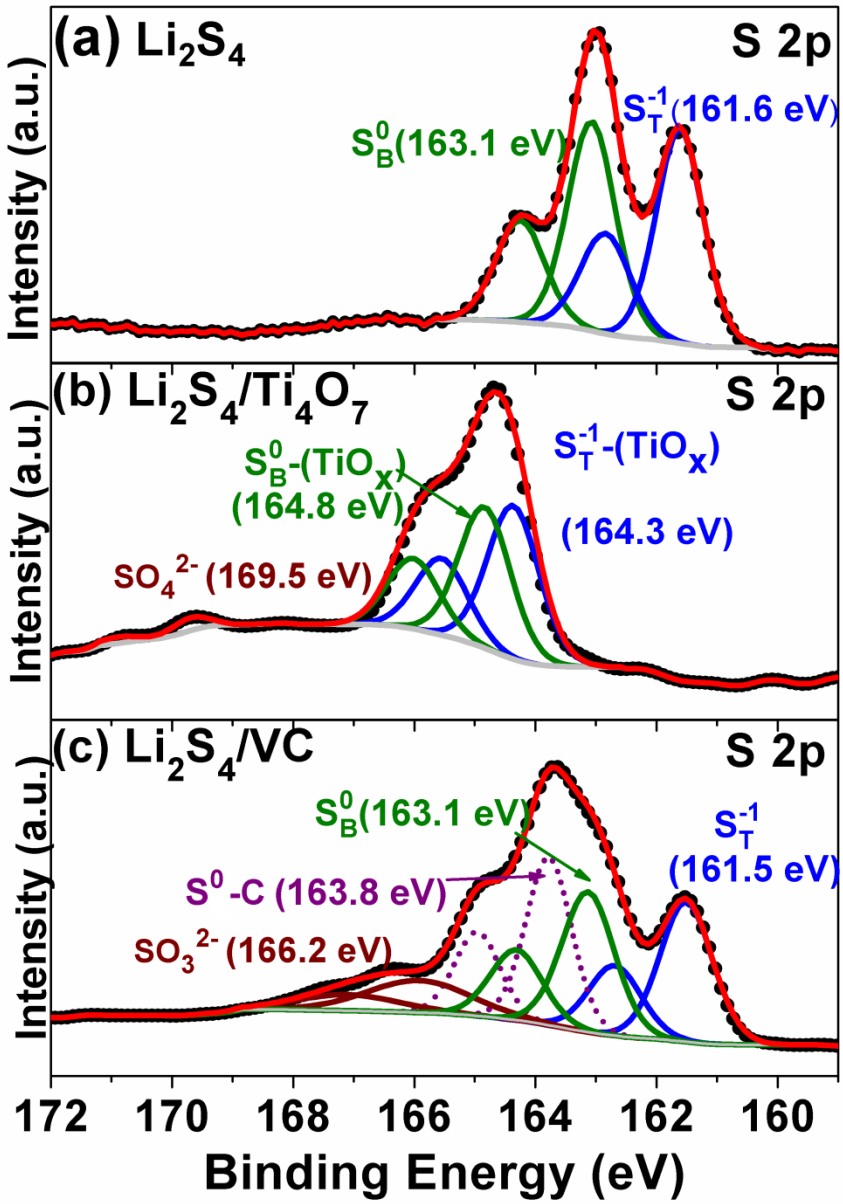

Figure 3.10 High-resolution XPS S 2*p* spectra of (a) Li_2S_4, (b) Li_2S_4/Ti_4O_7 and (c) Li_2S_4/VC. Black dotted line = experimental data, red line = overall fitted data, solid and dotted lines in other colors = fitted individual components.

The spectrum of Li_2S_4 bound to Ti_4O_7 is very different: it exhibits two higher binding energy $2p_{3/2}$ contributions at 164.3 and 164.8 eV (**Figure 3.10 b**), representing a +2.7 eV shift of the terminal S_T^{-1}, and a +1.7 eV shift of the bridging S_B^0. A similar binding energy (164.2 eV) has been attributed to interaction of elemental sulfur with the oxygen groups of graphene oxide.[25] Although the precise nature of the interaction with the reduced titanium oxide is not yet elucidated, the data clearly indicates that interaction of both the terminal and bridging sulfur of the LiPS with the surface of Ti_4O_7 results in polarization of electrons away from the sulfur atoms to the electropositive titania and/or oxygen vacancies at the interface (**Figure 3.11**). The terminal sulfur is more affected owing to its higher electron density. A minor, broad background bump between 166-169.5 eV is due to the formation of sulfite or sulfate[57] from a trace amount of water in the solvent. Also, in the Ti 2p spectrum of Li_2S_4/Ti_4O_7, compared with Ti_4O_7 (**Figure 3.12d,f**), there is a small shift towards lower binding energy by -0.2 eV, which is in accord with the positive shift of S 2p spectrum. This further confirmed the occurrence of electron density transfer from sulfide towards metal oxide. The shift is relatively small as electron density is not localized on the Ti atoms, but distributed over whole crystal, owing to the metallic bonding in the Ti_4O_7.

In contrast, Li_2S_4/VC shows a very similar S 2p spectrum to that of Li_2S_4 alone, with two sulfur contributions at 161.6 eV and 163.1 eV. This, along with the intense color in the Li_2S_4 solution even after long-term contact of the VC suggests that almost no adsorption occurs. The unaltered Li_2S_4 spectral features result from minor amounts of weak physisorption, in accord with their low intensity. An additional peak in the spectrum at 163.8 eV (**Figure 3.10c**) is in exact accord with the binding energy reported

for elemental sulfur supported on carbon (C-S^0).[25] Similar results were obtained for Li_2S_4/graphite (**Figure 3.12c**). This can be explained by the fact that where little or no interaction of polysulfides with the underlying support is present – as in the case of VC or graphite – the polysulfide species exist in rapid equilibria in solution. Anti-dismutase of intermediate-length LiPSs such as S_4^{2-} to lower and higher oxidation states of sulfur are known to occur under these conditions. Shifting of the equilibrium towards elemental sulfur formation is driven both by its insolubility and strong interaction with the carbon surface, thus accounting for the C-S^0 contribution. The accompanying (lower oxidation state) LiPS would not contribute significantly to the averaged spectrum (ie, that corresponds to Li_2S_{4-x}) as long as the extent of the anti-dismutase reaction remained minor. These findings are in full accord with the LiPS adsorption studies described above.

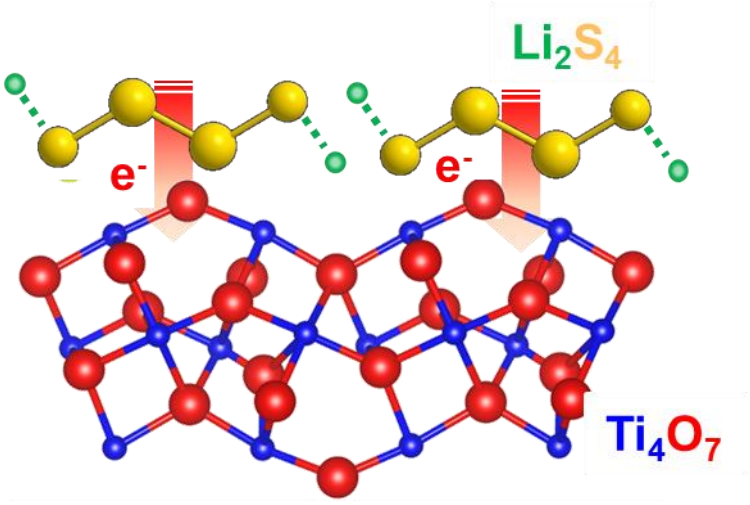

Figure 3.11 A schematic showing the electron density transfer between Li_2S_4 and a TiO_x surface that gives rise to the binding energy positive shift in S 2*p* spectrum (yellow = S, green = Li, blue=Ti, red = O).

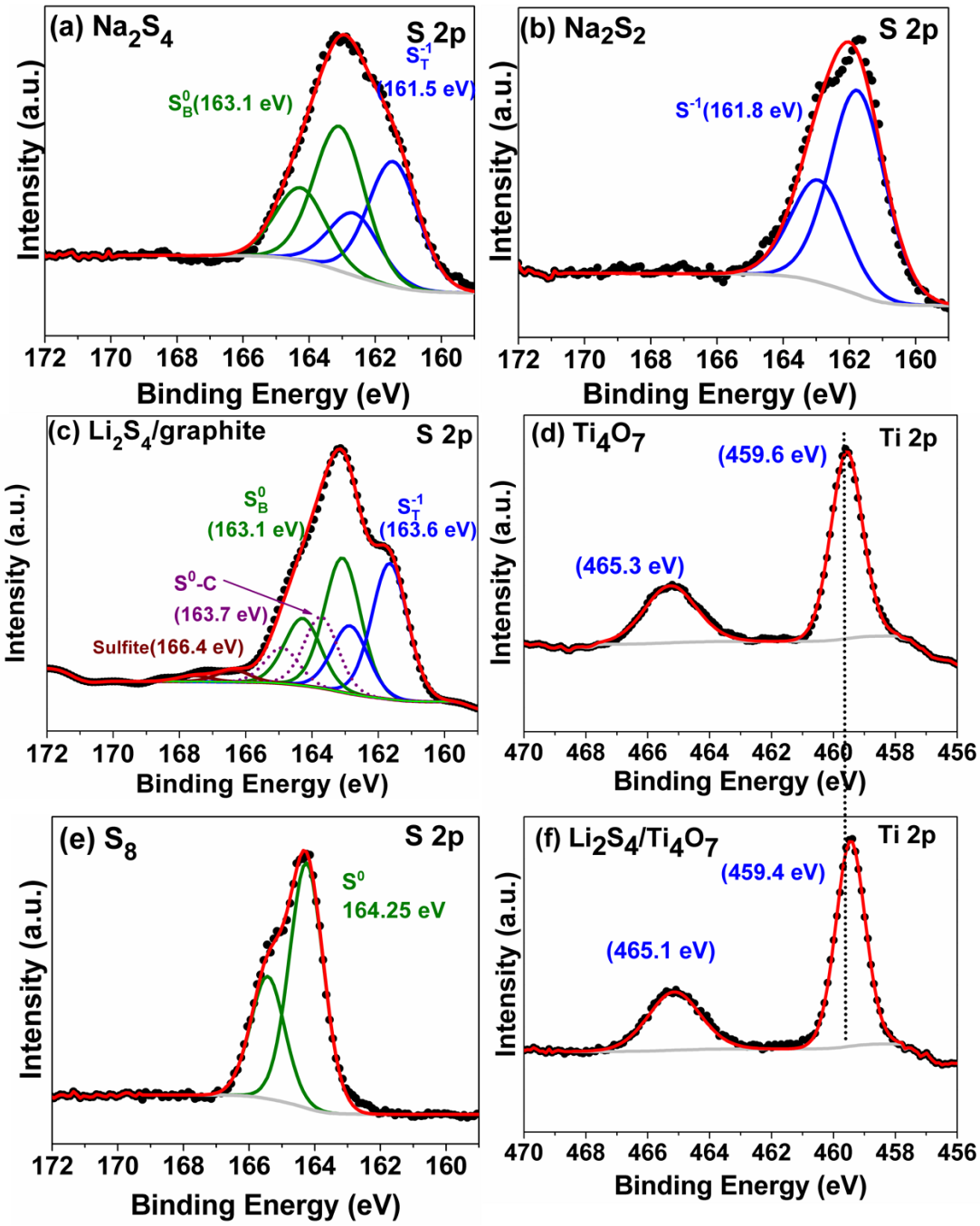

Figure 3.12 XPS S 2p core spectra of (a) Na_2S_2, (b) Na_2S_4, (c) S_8 and (d) Li_2S_4/graphite and Ti 2p spectra of (e) Ti_4O_7 and (f) Li_2S_4/Ti_4O_7 (black dotted line = experimental data, red line = overall fitted data, solid and dotted lines in other colors = fitted individual component, grey line = background).

3.3.3 Electrochemical studies

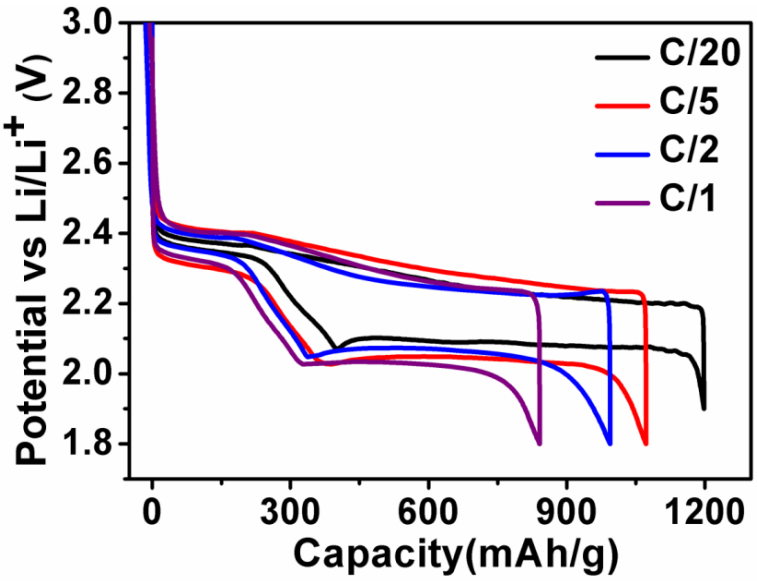

Figure 3.13 Discharge/charge voltage profiles of Ti_4O_7/S-60 cathodes at various rates.

The galvanostatic discharge/charge profiles of the Ti_4O_7/S-60 nanocomposite at different current densities (**Figure 3.13**) exhibit two typical well-defined plateaus at around 2.3 V and 2.1 V for discharge. No overcharge was observed during the first cycle, indicating the absence of a polysulfide shuttle. There is little increase in polarization with increasing rate, indicating favorable electrochemical kinetics owing to the high electronic conductivity of the Ti_4O_7 support and good electrolyte accessibility to the discharged/charged products within the cathodes. Two sulfur fractions (60wt% and 70wt%) were used to realize sulfur layers on Ti_4O_7 of various average thickness, in order to examine the effectiveness of the binding on cycling stability. Sulfur composite based on VC with 60 wt% sulfur was made in the same way as Ti_4O_7/S composites and denoted as VC/S-60. Better long-term cycling performance compared to VC/S-60 was evident

(**Figure 3.14**). The Ti_4O_7/S-60 cell experienced very stable capacity retention over 250 cycles at C/2 with an average fade rate as low as 0.078% per cycle, whereas the VC/S-60 cell faded at twice the rate, 0.150% per cycle.

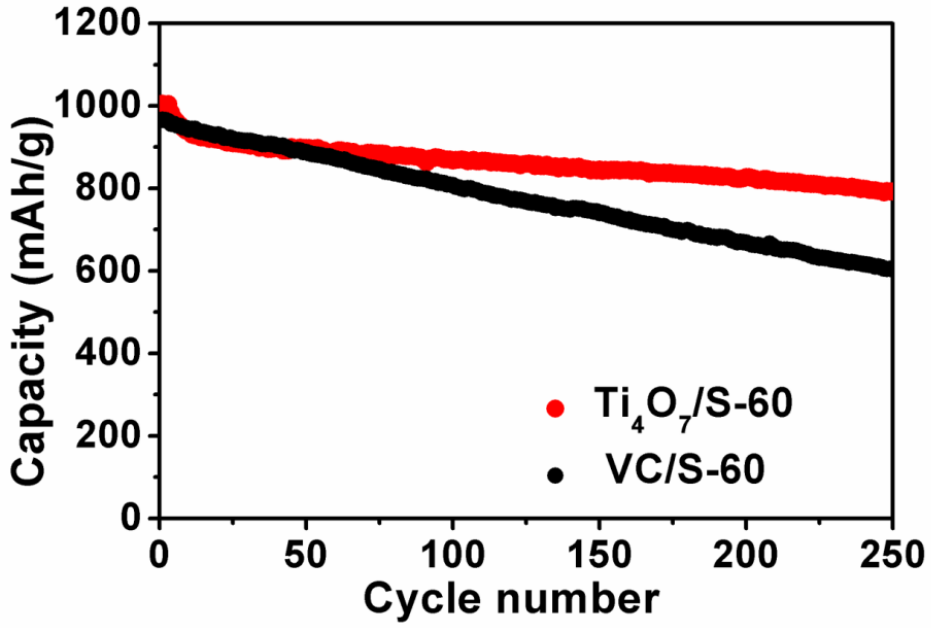

Figure 3.14 Cycle performances of Ti_4O_7/S-60 and VC/S-60 at C/2 over 250 cycles.

With high fraction of sulfur up to 70 wt% for Ti_4O_7/S composites, the cathode exhibited identical performance with ~80% capacity retention at C/2 over 100 cycles (**Figure 3.15 a**), indicating the strong adsorption ability of Ti_4O_7 for LiPSs. High-rate cycling at 2C (with activation at C/20 before cycling) yielded a high initial capacity of 850 mA h/g with an average fade of only 0.072% per cycle over 500 cycles (**Fig. 3.15b**). At relatively lower rate C/5, excellent capacity retention of 88% over 100 cycles was also observed (**Figure 3.15a**).

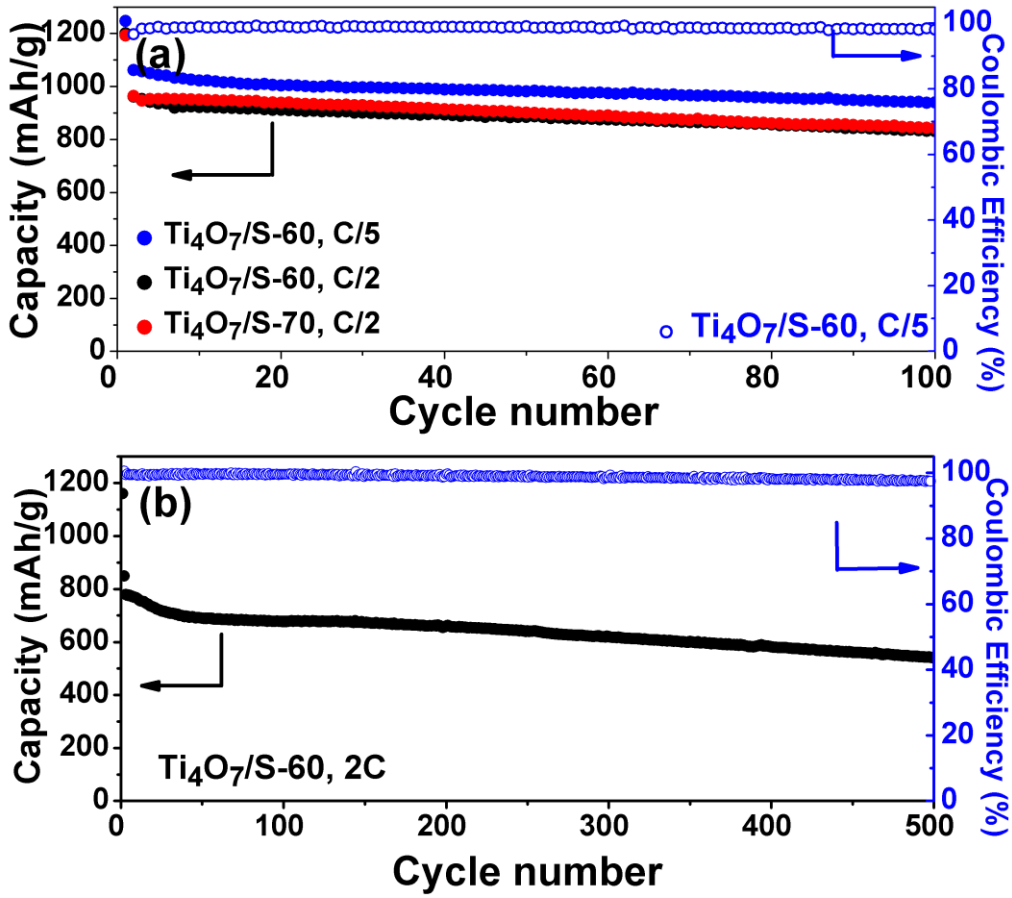

Figure 3.15 (a) Cycle performances of Ti_4O_7/S nanocomposites with different sulfur fractions at C/5 or C/2 over 100 cycles with CE shown for Ti_4O_7/S-60 at C/5 as a representative. (b) High-rate cycle performance of Ti_4O_7/S-60 at 2C over 500 cycles with corresponding CE.

CV measurements carried out on Ti_4O_7/S-60 and VC/S-60 electrodes revealed additional differences in the properties of the two materials. Both show a typical profile that displays two cathodic peaks and a broader anodic peak (**Figure 3.16**), which correlate with the previously described plateaus in the galvanostatic voltage profiles (**Figure 3.13**). However, the electrochemical response is significantly more diffuse in the case of Ti_4O_7 for both the cathodic and anodic sweeps, exhibiting less of a solution-like

behavior as characterized by the narrow peaks as in VC/S-60. Since the mass transport kinetics would be expected to be the same, the increased breadth of the redox peaks appears to reflect a surface-mediated interaction which is stronger for Ti_4O_7/S-60. Furthermore, after three cycles, the cathodic and anodic currents stabilized during the 15 measurement cycles, whereas those for the VC/S-60 continuously dropped (**Figure 3.16, insets**).

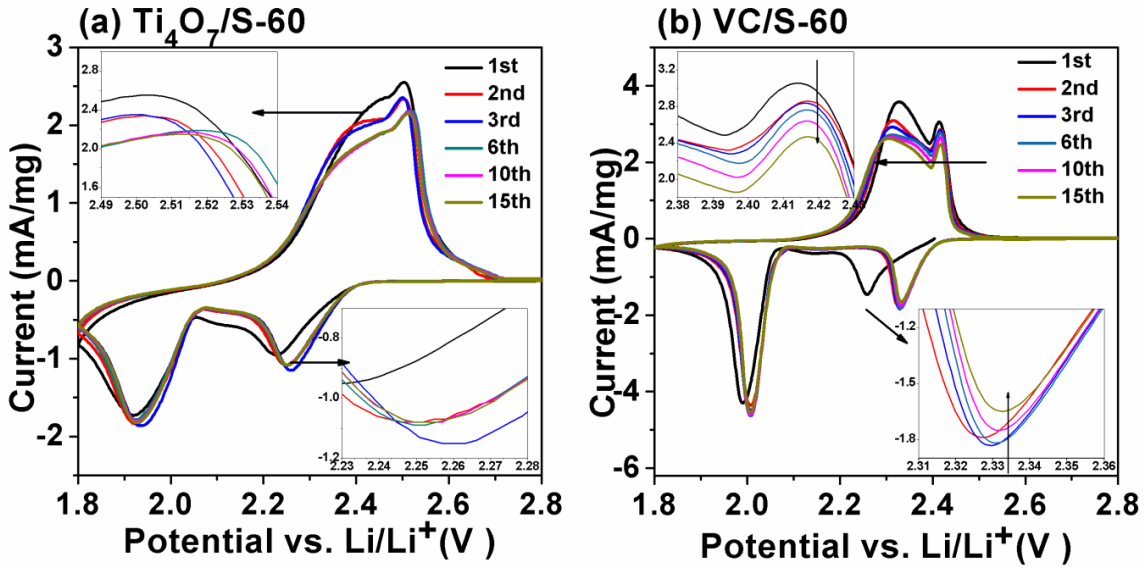

Figure 3.16 Representative CV curves for (a) Ti_4O_7/S-60 cell and (b) VC/S-60 cell at 0.1 mV/S sweeping rate for the first 15 cycles. The insets are magnified curves around the anodic peak and the high-voltage cathodic peak. The currents are normalized by the mass of sulfur loading on the electrodes.

3.3.4 Electrode nanostructure and impedance evolutions upon cycling

The underlying reason for the stable capacity delivery was further explored by examining the cathode nanostructure evolution over cycling. Cycled cells stopped at different discharged/charged points were disassembled and examined by SEM. Figure

3.17a,d show the images for the pristine Ti_4O_7/S-60 and VC/S-60 electrodes, respectively. On the first discharge, although an expanded and glassy layer of Li_2S is evident on the surface of the particles in both cases, the underlying particles are more defined for the Ti_4O_7 host (**Figure 3.17b,e**), suggestive of the conformal deposition of Li_2S on the surface (*ie*, the result of better wetting). In contrast, the Li_2S on carbon is broadly and non-specifically distributed.

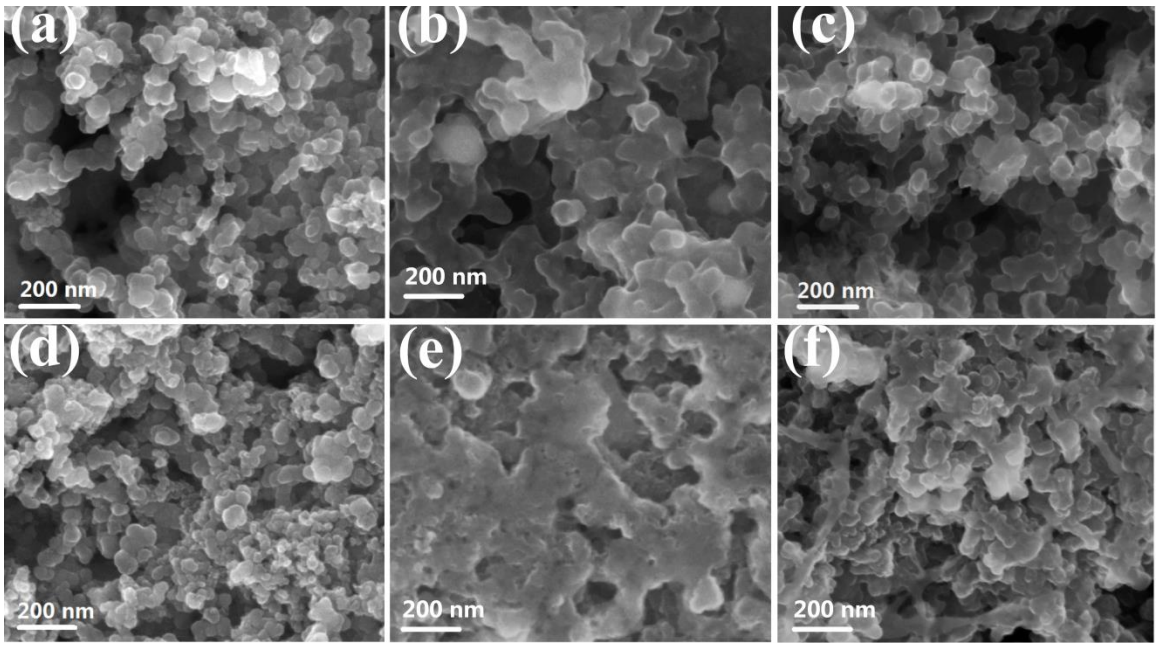

Figure 3.17 SEM images showing the pristine cathodes (a,d) and cathodes after 1st discharge (b,e) and after 500 cycles at charged status (c,f) for Ti_4O_7/S-60 (a,b,c) and VC/S-60 (d,e,f).

EIS spectroscopy on the cycled electrodes lends additional support to the above argument (**Figure 3.18 a,b**). These studies provide measure of the charge-transfer resistance at the positive (or negative) electrode interface resulting from deposition of products on discharge or charge.[58] The Nyquist plot was fitted using the equivalent circuit

shown in **Figure 3.19**. On the first discharge, the Ti_4O_7/S-60 cell (**Figure 3.18a**) exhibits a charge-transfer resistance in the high-intermediate frequency range (R_1+R_2, attributable to the positive electrode) that is two-fold lower that of the VC/S-60 (**Figure 3.18b**). This difference is starkly evident from a comparison of the two plots. We ascribe this to the enhanced interaction of the LiPSs - and subsequently the Li_2S - with Ti_4O_7, in full concert with the findings from the SEM data. As expected, the non-specific precipitation of Li_2S on the carbon-based electrode gives rise to higher resistance, but in contrast, charge transfer at the ionic Li_2S - Ti_4O_7 interface is more efficient.

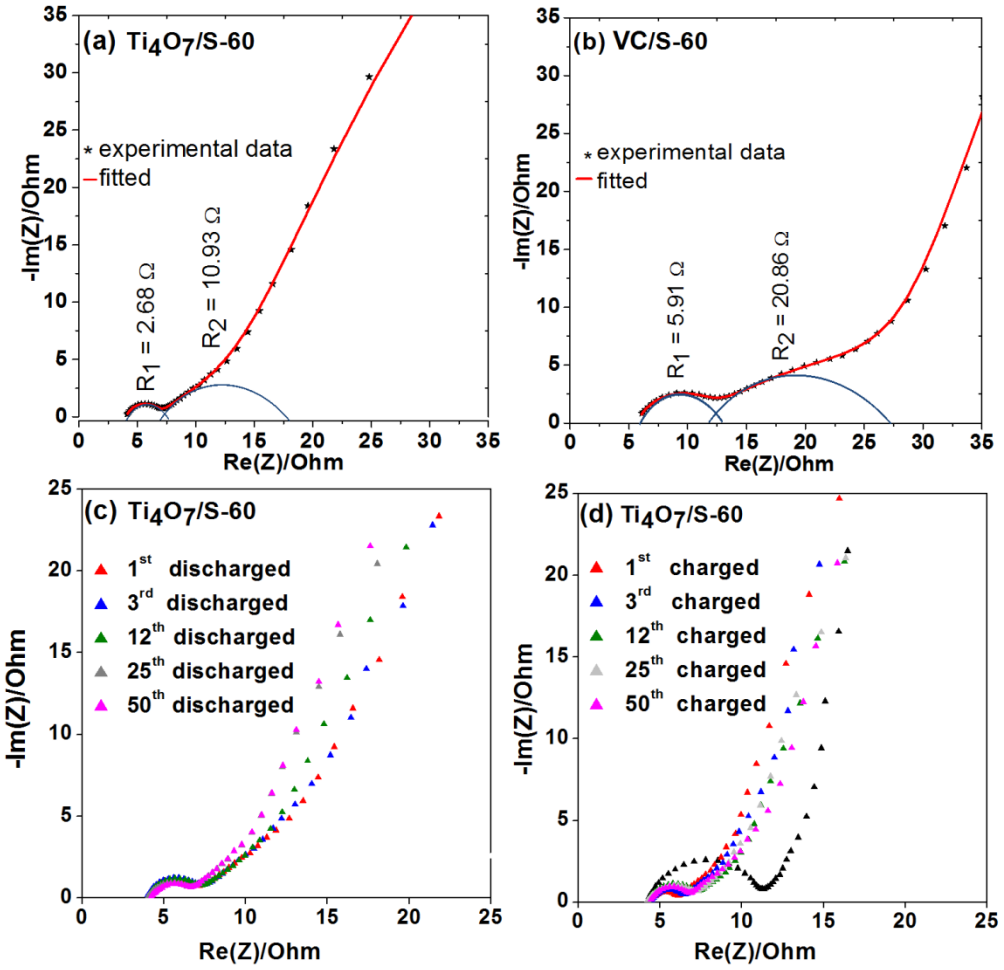

Figure 3.18 Nyquist plots of (a) Ti_4O_7/S-60 and (b) VC/S-60 cells at discharged status on the 1st cycle at a C/2 rate; and Ti_4O_7/S-60 at (c) discharged, (d) charged status after 50 cycles at a C/2 rate. Fitted resistance values for (a) and (b) correspond to the equivalent circuit shown in Figure 3.19.

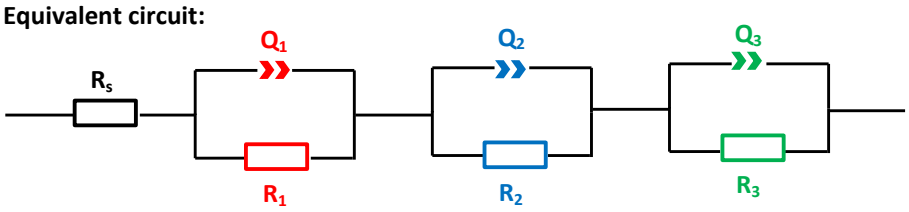

Figure 3.19 Equivalent circuit used for EIS fitting in Figure 3.18a and b. Constant phase element (Q) was used to represent the non-ideal behavior of the system, as reflected by the depressed semicircles.

After the fifth charge or discharge, the Ti_4O_7/S-60 cathode exhibited a very similar morphology to the pristine electrode, i.e. sulfur or Li_2S was redeposited onto Ti_4O_7 support uniformly (**Figure 3.20 a, b**). Even after 500 cycles at C/2, the particle-like morphology was still largely preserved for Ti_4O_7/S-60. In accord, EIS spectra at both discharge and charge over 50 cycles show negligible change (**Figure 3.18c, d**). This suggests little variation in the electronic conductivity and charge-transfer resistance with excellent nanostructure integrity over cycling. In contrast, a more densely distributed product (sulfur and/or Li_2S) was precipitated out for the VC/S-60 cathode (**Fig. 3.17e, f**). It has been shown that Li_2S particles easily detach from typical carbon electrode surfaces, which can lead to loss in electrical contact.[29]

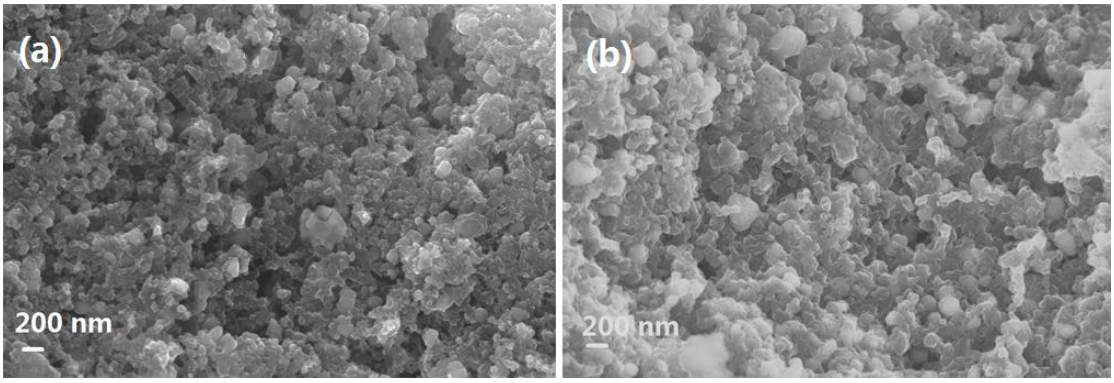

Figure 3.20 SEM images of Ti_4O_7/S-60 after 6th charge (a) and discharge (b).

Based on the observations discussed, the mechanism for more uniformed and confined deposition of Li_2S, better electrode integrity and improved cycle performance for Ti_4O_7 compared with carbon is proposed as shown in **Figure 3.21**. During discharge, when sulfur on Ti_4O_7 surface takes electrons and Li^+ ions from Ti_4O_7 and electrolyte, the as-formed Li_2S_6/ Li_2S_4 molecules are adsorbed on the Ti_4O_7 surface for and upon further reduction to Li_2S, it is effectively adsorbed on Ti_4O_7 as well (**Figure 3.21a**), promoting electric contact and inhibiting polysulfide diffusion. In contrast, for carbon support, due to the lack of absorption for LiPSs, Li_2S_6/ Li_2S_4 are diffused into electrolyte and Li_2S is detached from support (**Figure 3.21b**), forming a Li_2S layer on the electrode surface. More importantly, the dissolution of LiPSs can lead to polysulfide shuttle, causing capacity fading.

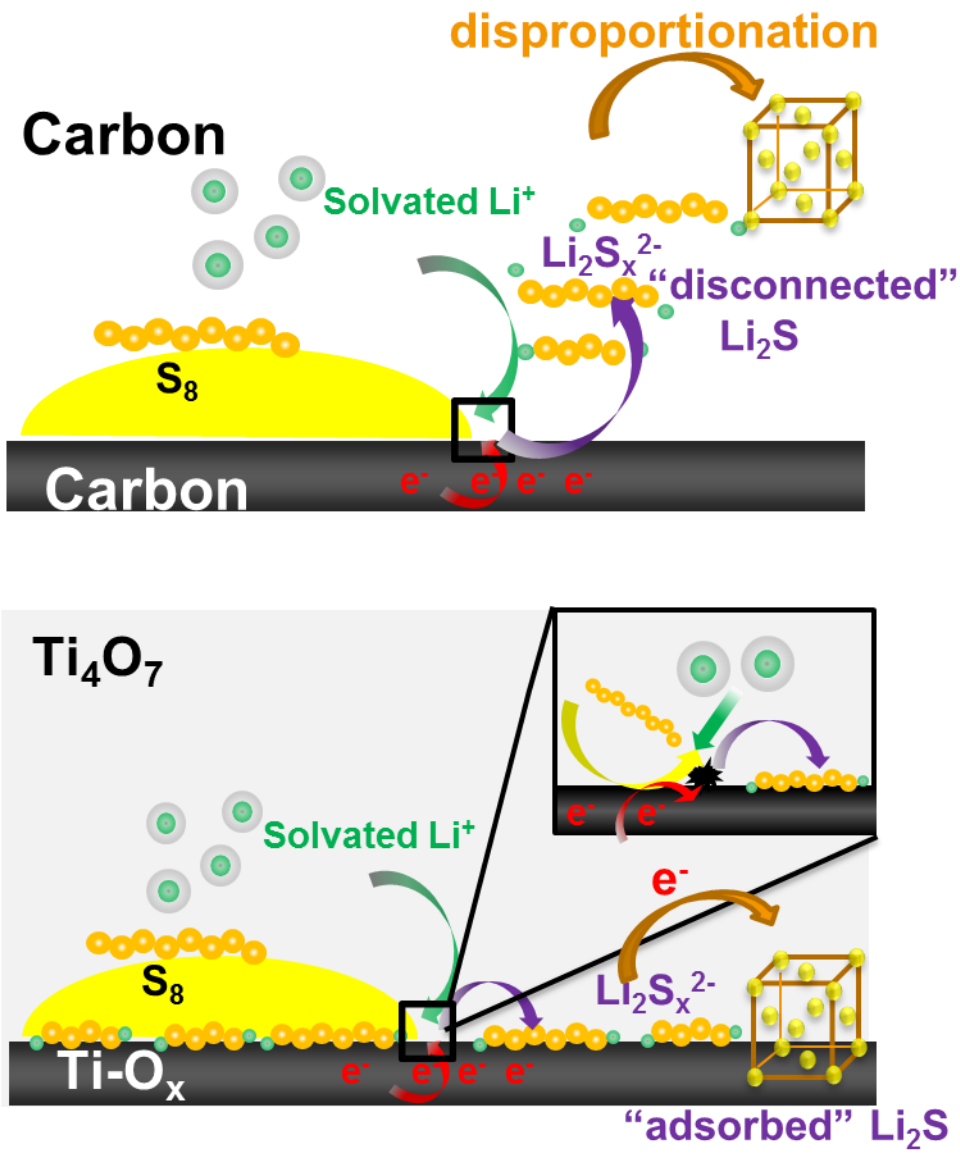

Figure 3.21 Schematic illustrations on the sulfur reduction processes on carbon support (a) *vs.* Ti_4O_7 support (b). $Li_2S_x^{2-}$ intermediates are adsorbed on the Ti_4O_7 surface, while for carbon, they diffuse into the electrolyte during discharge.

3.4 Conclusion

In this chapter, I have demonstrated a new class of sulfur host materials that combine electronic conductivity for redox electron transfer with a polar surface for strong polysulfide/Li_2S binding. This provides a bifunctional cathode material for Li-S batteries that enables low capacity fading rates over long-term. The interaction between Ti_4O_7 and LiPS was probed using XPS analysis. A binding energy shift towards higher value for S *2p* spectrum indicates the electron transfer from bridging and terminal sulfur to Ti_4O_7 surface. The novel sulfur host material has a high surface area and pore volume to support up to 70 wt% of sulfur, and as low as 0.078% capacity loss per cycle was obtained at high rate C/2. By investigating the electrodes after different numbers of cycles, it is shown that the morphology integrity for Ti_4O_7/S-60 composite is much improved, compared with VC/S-60, due to the better wetting of LiPSs and Li_2S. In addition, because Ti_4O_7 has a more than three-fold higher density than typical amorphous carbons (4.32 cc g^{-1} *vs* ~1.2 cc g^{-1}), the volumetric energy density of the overall cathode composite is also increased. The concept extends not only to Ti_4O_7 and other members of the Magnéli phase family, but is also widely applicable to conductive materials with intrinsic polar characteristics. A paper based on this work has been submitted [59] and also, an intellectual property disclosure by the Waterloo Commercialization Office is under preparation.

Chapter 4 Synthesis of nanostructured MgB_2 and its application in sulfur cathode

4.1 Introduction

4.1.1 Metallic property of MgB_2

The binary intermetallic compound MgB_2 is mostly used as a high transition temperature superconductor. It has a simple hexagonal layered structure (AlB_2 type, P6/mmm), with lattice parameters of a = 3.086 Å and c = 3.524 Å, as shown in **Figure 4.1**. Boron atoms form a primitive honeycomb lattice, consisting of graphene-type sheet layers stacked with no interlayer displacement. Closely packed Mg atoms form a layer between the adjacent B layers. As seen from the lattice parameters, the intraplanar B-B bonds are much shorter than the distance between interplanar B atoms. Bonding within the B layers is mostly covalent bond with sp^2 hybridization, but bonding between B-Mg layers is ionic as explained below.[60,61] The presence of a Mg layer between the B layers enhances the interlayer overlap and strong hybridization between dangling B $2p_z$ and Mg 3*s* orbitals. This causes the Mg 3*s* orbital to shift upward and the B $2p_z$ orbital to shift downward relative to their elemental states. Due to these shifts, electrons in the Mg 3*s* orbital are partially donated to B $2p_z$ and Mg becomes positively charged. However, the electrons donated are not localized on the adjacent B atoms, but rather distributed over the whole crystal, i.e. B-Mg interlayers, forming a big π bond like graphite.[62] Therefore, MgB_2 has electronic conductivity of as high as 10^4 S cm^{-1}, as reported in some polycrystalline samples. [63,64]

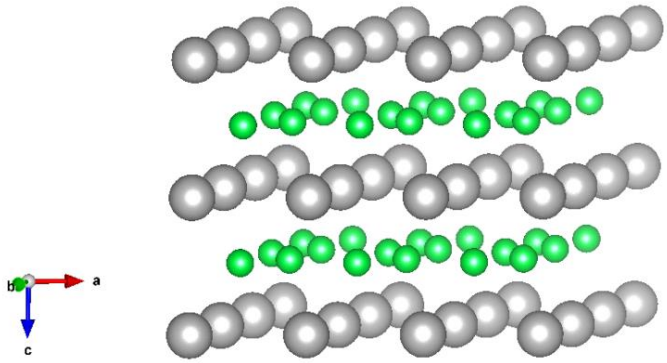

Figure 4.1 Schematic illustration of crystal structure of MgB_2 (grey = Mg, blue= B).

4.1.2 Use of MgB_2 as a sulfur host material

As mentioned above, MgB_2 has high conductivity, satisfying the role of conducting electrons for sulfur redox reactions. More importantly, since the Mg atom bears a formal positive charge rendering MgB_2 a polarized/ionic structure, MgB_2 is expected to adsorb hydrophilic LiPSs via electrostatic forces. Ideally, if high-surface area MgB_2 is in intimate contact with elemental sulfur, LiPSs formed during cycling are likely to be trapped on the surface of MgB_2, thus preventing the loss of active materials. In addition, one advantage of MgB_2 over Ti_4O_7 in **chapter 3** is its light weight with an average atomic weight of 15.3 g mol^{-1}, which is comparable to carbon (12 g mol^{-1}). This can be seen from comparison of the theoretical bulk density as well ($\rho(MgB_2)$ = 2.57 g cm^{-3}, ρ(graphite) = 2.23 g cm^{-3}). Therefore, if MgB_2 is used instead of carbon, the gravimetric capacity of the whole electrode will not be much affected.

MgB_2 has been intensively explored as a high transition temperature superconductor in bulk forms. Very few literature has been published on the synthesis of nanoscaled MgB_2.[65,66] The main hurdle of preparing pure-phase MgB_2 lies on the fact that

Mg is very reactive towards oxygen at elevated temperatures, thus the control of atmosphere during high temperature treatment is extremely important. In this chapter, the synthesis of both bulk and nanostructured MgB_2 and their application as sulfur host materials were explored.

4.2 Bulk MgB_2 prepared via $Mg(BH_4)_2$ decomposition

4.2.1 Experimental

MgB_2 has been prepared from thermal decomposition of $Mg(BH_4)_2$ in some reports, [67] because $Mg(BH_4)_2$ is an excellent source providing Mg and B at a ratio of 1:2 mixed at atomic level. Accordingly, a method modified in treatment temperature was adopted for synthesis of MgB_2 in this section. Inside glovebox, commercial $Mg(BH_4)_2$ powder was loaded onto a nickel boat and put into a steel tube under Ar. The tube was closed on one end and the other end was connected to dynamic vacuum (10^{-5} Torr). The sample was sintered at 480 ^{o}C under vacuum for 0.5 hour with a ramp rate of 15 ^{o}C/min. The as-synthesized MgB_2 (denoted as bulk-MgB_2) was stored in glovebox to minimize possible air oxidation.

4.2.2 Physical characterizations

The XRD pattern of the black powder obtained is shown in **Figure 4.2**. It confirms a dominant phase of MgB_2 with a small percentage of MgO, probably on the surface due to trace amount of oxygen present in the reactor. The SEM images in **Figure 4.3a, b** reveal the bulk structure of MgB_2, which consists of large particles with rough surface. EDX analysis in **Figure 4.3c,d** demonstrates the existence of Mg, B and O, also

indicating the formation of MgO. The morphology of bulk-MgB_2 is expected to be similar with that of the precursor $Mg(BH_4)_2$. Low temperature decomposition was used to minimize particle growth.

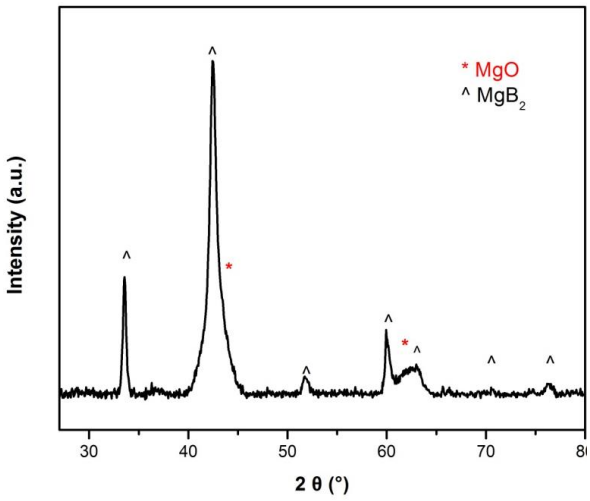

Figure 4.2 XRD pattern of bulk-MgB_2 synthesized via decomposition of $Mg(BH_4)_2$.

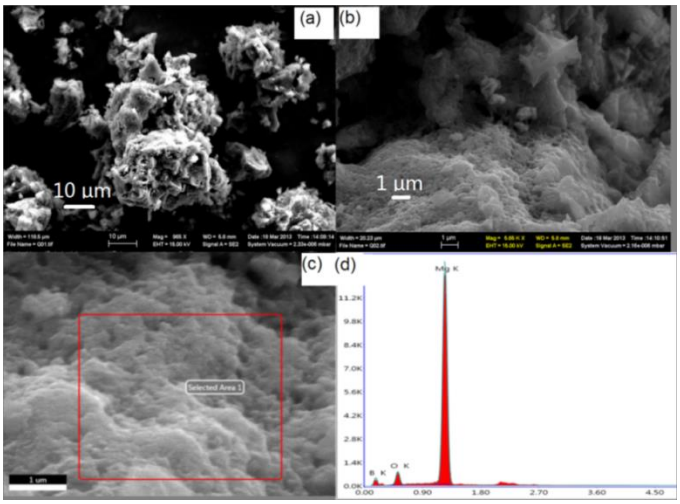

Figure 4.3 (a, b, c) SEM images of bulk-MgB_2 synthesized from thermal decomposition of $Mg(BH_4)_2$ at different magnifications and (d) EDX spectrum of the area in red square of image (c).

4.2.3 Electrochemical measurements

Bulk-MgB_2/S composites with 50 wt% and 75 wt% of sulfur (denoted as bulk-MgB_2/S-50 and bulk-MgB_2/S-75) were prepared with the assistance of toluene. Typically, toluene solution of sulfur (5 mg/mL) was stirred with desired amount of MgB_2 for 3 hours, followed by toluene evaporation at 80 ^oC overnight inside the glovebox. The positive electrodes were constructed with (80 wt%) bulk-MgB_2/S, (10 wt%) polytetrafluoroethylene binder and (10 wt%) Super P. The mixture was dispersed in DMF to form slurry that was drop-cast on P50 carbon paper. The cell was assembled inside a glovebox, with lithium metal as anode, and 1 M LiTFSI and 2wt% of $LiNO_3$ in a mixture of DME and DOL (v:v = 1:1) as electrolyte.

The galvanostatic discharge/charge profiles of bulk-MgB_2/S-50 at C/10 and C/2 (**Figure 4.4a**) exhibit normal voltage profile of Li-S battery with two plateaus for discharge, indicating MgB_2 is electrochemical inactive during the voltage window (1.8 - 3 V). Initial discharge capacities of 1358 and 1022 mA h/g were achieved at C/10 and C/2, respectively. In terms of long-term cycling (**Figure 4.4b**), the bulk-MgB_2/S-50 composite remained 54% and 74% of initial capacity over 200 cycles at C/10 and C/2, respectively. The lower rate gave rise to higher initial capacity but higher fading rate. In addition, by increasing the sulfur fraction to 75 wt%, high initial capacity of 1134 mA h/g with 68% retention were achieved over 200 cycles at C/5 (**Figure 4.4b**).

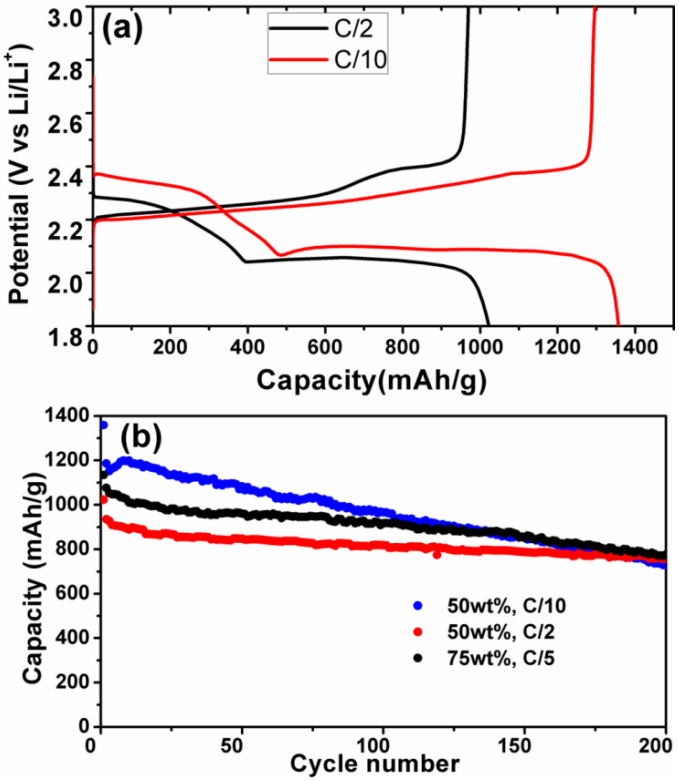

Figure 4.4 (a) Galvanostatic voltage profiles of bulk-MgB_2/S-50 composite at C/10 and C/2. (b) Cycle performance of bulk-MgB_2/S-50 at C/2, C/10 and bulk-MgB_2/S-75 at C/5 over 200 cycles.

In summary, bulk form MgB_2 was synthesized in a facile way from $Mg(BH_4)_2$ thermal decomposition. Despite its low surface area, prolonged cycle performance based on bulk MgB_2 was demonstrated over 200 cycles. With a higher surface area for MgB_2 as in the next section (Section **4.3**), better electrochemical performances can be achieved.

4.3 Nanosized MgB_2 prepared via solid-state reaction

4.3.1 Experimental

The nanosized MgB_2 was synthesized by solid state reaction between elemental Mg and B. By exposure of B powder to Mg vapor, MgB_2 can be obtained via a diffusion-based reaction.[68] Nanosized B powder is commercially available and with the heating parameters appropriately handled, nanosized MgB_2 can be obtained with similar morphology as the starting B precursor. In a typical synthesis, Mg metal powder confined in a pellet and B nanopowder (~50 nm) were put at each end of a Ta tube (~12 mm diameter, ~60 mm long), which was then sealed under Ar using an electric arc furnace. Since MgB_2 is the one with the highest Mg fraction in stoichiometry among all magnesium borides (other include MgB_4, MgB_6 and MgB_{12}), excess Mg with a Mg : B atomic ratio of 1.1 : 2 was used, in order to obtain MgB_2 phase and make sure B is completely reacted. The Ta tube was then sintered under Ar flow in a tube furnace. The heating temperature was ramped to 700 ^{o}C (10 ^{o}C/min) and stayed for 2 hours, followed by a further ramp to 950 ^{o}C (6 ^{o}C/min) for 6 hours. The Ta tube was cooled down and opened in a glovebox for characterization. The as-synthesized MgB_2 was denoted as nano-MgB_2.

4.3.2 Physical characterizations

There are two reasons why a Ta tube was used in this synthesis approach. First, Ta is oxygen free (unlike quartz tube) so that oxygen contamination from the "reactor" can be avoided. Second, Ta is easy to seal. An Ar atmosphere/flow both inside and outside of the tube was applied to exclude any possible oxygen contamination. The

heating stage at 700 ^{o}C allows the Mg metal to melt and vaporize, creating uniform Mg atmosphere, while still keeping the temperature low to inhibit particle growth.

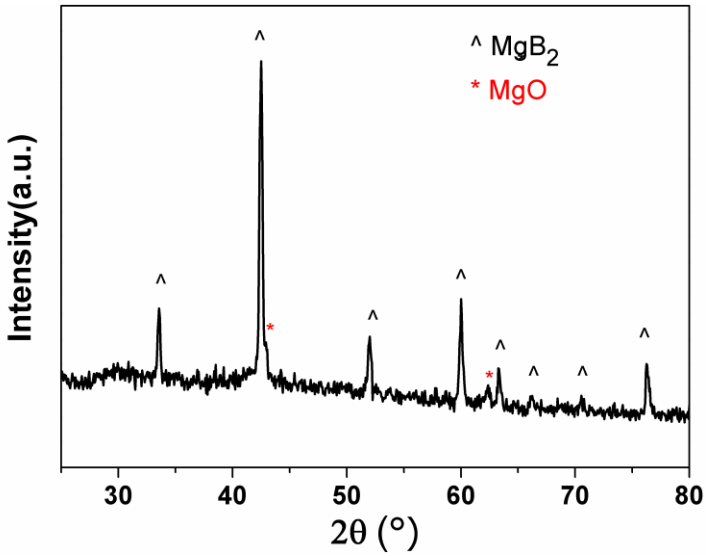

Figure 4.5 XRD pattern of nano-MgB_2 synthesized by solid-state reaction between boron nanopowder and Mg.

The XRD pattern of nano-MgB_2 is shown in **Figure 4.5**. Crystalline MgB_2 was confirmed to be the primary phase, with a small amount of MgO. SEM studies were carried out to investigate the particle morphology. Uniform interconnected particles of ~400 nm were formed as seen in **Figure 4.6a, b**. During the sintering, B particles grew significantly upon exposure to Mg and as-formed MgB_2 were sintered together to form a "network". This network can both increase the overall conductivity and provide porous architecture to physically confine LiPSs. There is a question as to whether there was unreacted amorphous B left in the sample. The B nanopowder was composed of ~50 nm particles as seen in **Figure 4.6c**. Absence of small particles (<100 nm) in nano-MgB_2 suggests there was no unreacted B left. The bright-field TEM image shown in **Figure**

4.7a is consistent with SEM imaging regarding particle morphology. The selected area electron diffraction (SAED) pattern in the inset of **Figure 4.7b** further confirms a hexagonal lattice corresponding to MgB_2.

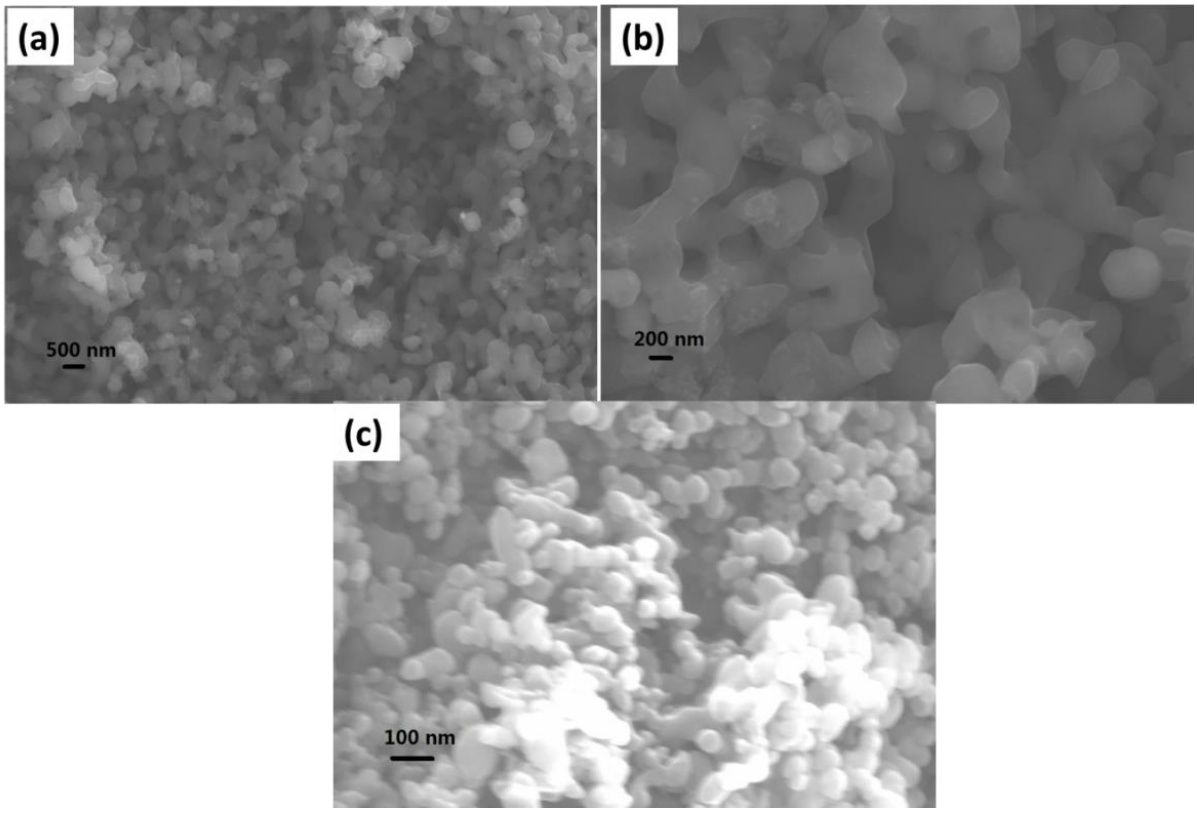

Figure 4.6 (a,b) SEM images of nano-MgB_2 synthesized by solid-state reaction between boron nanopowder and Mg at lower (a) and higher (b) magnification. (c) SEM image of commercial boron nanopowder.

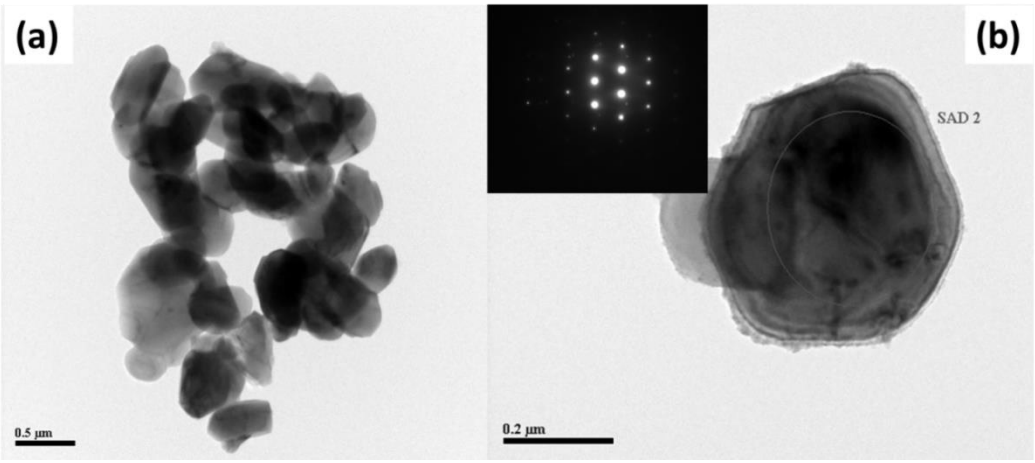

Figure 4.7 (a,b) Bright-field TEM images of nano-MgB_2 synthesized by solid-state reaction between boron nanopowder and Mg at lower (a) and higher (b) magnification, with the SAED pattern of circled area in the inset of (b).

4.3.3 Carbon nanotubes to inhibit particle growth

Particle growth during high temperature solid-state synthesis is indeed a problem in order for small particle size. There are basically two ways to alleviate this problem. One is to adjust the heating temperature and duration; the other is to use an additive to spare the heat from aimed particles or to act as a capping agent. In this section, carbon nanotubes (CNTs, ~8 nm diameter) was used as an additive, along with temperature control. Typically, CNTs was first ball-milled with B nanopowder under Ar at 300 rpm for 1 hour to mix thoroughly. The mixture was then reacted with Mg in the same way as in the last section. The amount of carbon in the final composite was set to be 20 wt%. Sintering temperature of 800 ^{o}C in addition to 950 ^{o}C was used.

XRD analysis was conducted on the samples for phase identification. Sample sintered at 950 ^{o}C was confirmed to be a mixture phase of MgB_2C_2 and MgB_2 (XRD

pattern is not shown here). The MgB_2C_2 phase formed probably due to increased reactivity of carbon with Mg at elevated temperature. Therefore, lower temperature at 800 ^oC was tried. The XRD pattern in **Figure 4.9a** shows that MgB_2 is the dominant crystalline phase (with trace amount of MgO) without MgB_2C_2 at lowered temperature. This sample is denoted as nano-MgB_2/CNT. The coherence length of nano-MgB_2/CNT, as calculated via Scherrer equation (**Equation 2.2**), is ~17 nm, whereas that of nano-MgB_2 is ~27 nm, indicating smaller domain size for nano-MgB_2/CNT. The SEM image in **Figure 4.9b** also demonstrated much smaller particle size ~100 nm using CNTs additive. This is advantageous in providing higher surface area for binding LiPSs .

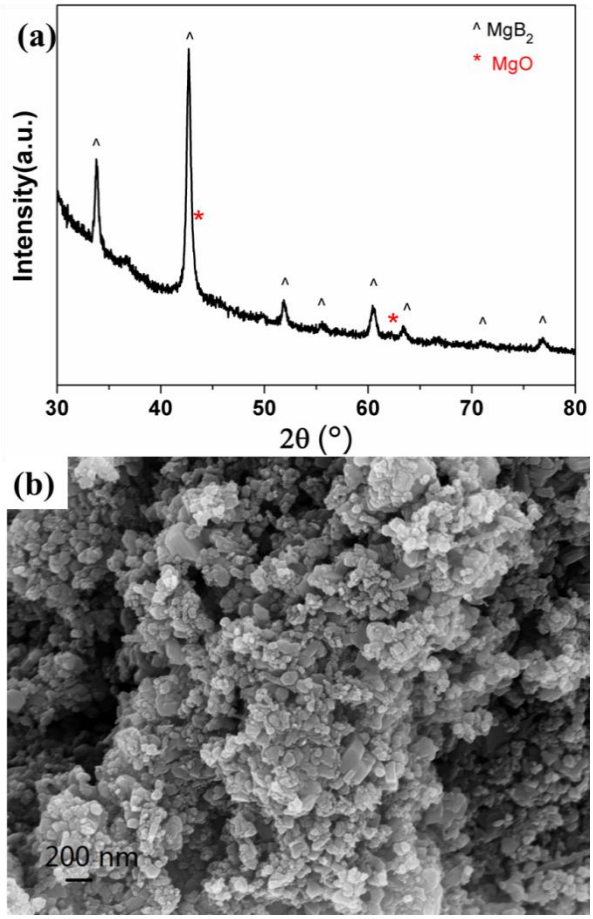

Figure 4.8 (a) XRD pattern and (b) SEM image of nano-MgB_2/CNT.

In order to inspect into the surface compositions, high-resolution XPS analysis on B 1*s* and Mg 2*p* regions were carried out. It is observed from B 1*s* spectrum (**Figure 4.9a**) that there are two B components, positioned at 187.3 eV (71 at%) and 191.3 eV (29 at%), corresponding to the B_2Mg and borate ($B_xO_y^{n-}$)/boride species,[57,69] respectively. The peak at 187.3 eV lies within the range of binding energy of common transition metal borides.[70] The analysis indicates absence of elemental B, but there was oxidation of B on the surface. For Mg *2p* spectrum, two peak positioned at 49.3 eV (27 at%) and 50.5 eV (74 at%) were observed. There is yet no universal agreement on the exact valence state of Mg and Mg 2*p* binding energy in MgB_2, as it is difficult to synthesize pure MgB_2.[69] Some reports support that Mg in MgB_2 bears less than +2 charge, whereas Mg in MgO bears +2 obviously.[70] Based on this, the peak with lower binding energy at 49.3 eV is assigned to MgB_2, while the one at 50.5 eV represents MgO (also confirmed from XRD pattern in **Figure 4.8a**). The two assignments also agree with the values reported in references 55 and 66. Therefore, it can be concluded that a large percentage of MgO exists on the surface. This inevitable oxidation may benefit on electrochemistry, *i.e.*, MgO on the surface might have stronger absorption ability for LiPSs as reported previously,[71] while highly conductive and interconnected MgB_2 can provide overall conductivity.

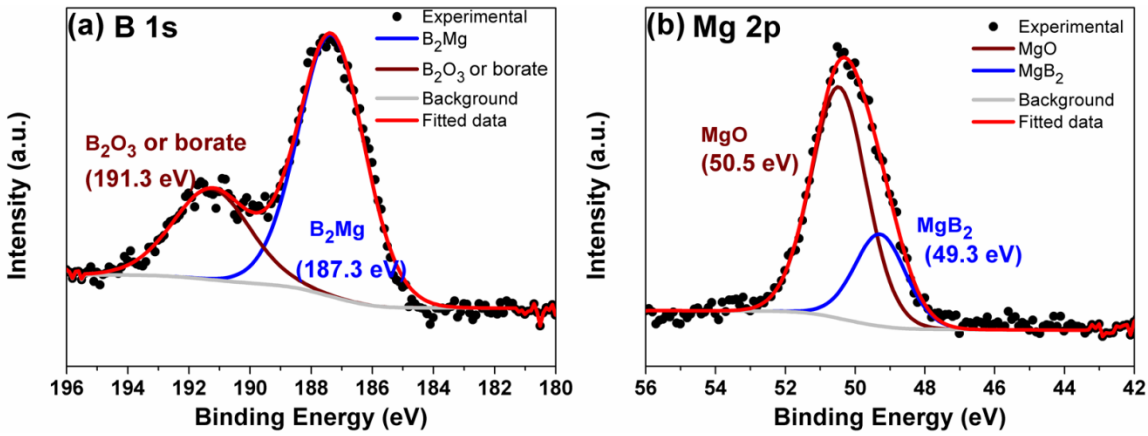

Figure 4.9 High-resolution XPS spectra of nano-MgB_2/CNT at the regions of (a) B 1*s* and (b) Mg 2*p*.

4.3.4 Electrochemical measurements

Since nano-MgB_2/CNT has the smallest particle size, it was utilized as sulfur host for electrochemical measurements. Melt-diffusion method was used to impregnate 60 wt% of sulfur into as-synthesized nano-MgB_2/CNT. The positive electrode was constructed with (80 wt%) nano-MgB_2/CNT/S-60, (10 wt%) PVDF binder and (10 wt%) CNTs. The mixture was dispersed in DMF to form slurry that was drop-cast on P50 carbon paper. The cell was assembled with lithium metal as anode, and 1 M LiTFSI and 2 wt% of $LiNO_3$ in a mixture of DME and DOL (v:v = 1:1) as electrolyte.

The discharge/charge voltage profiles of initial cycle at C/2 and C (after an activation cycle at C/10) are shown in **Figure 4.10a**. An initial capacity of 985 and 786 mA h/g were achieved at C/2 and C with minimum overcharge, respectively. The over-potential at the beginning of charge is negligible, indicating optimized Li_2S deposition on MgB_2 support (or probably MgO), which reduced the electrode resistance. Excellent long-term cycle performance at C/2 was demonstrated in **Figure 4.10b**. With an initial

capacity of 985 mA h/g, 774 mA h/g was retained over 200 cycles, corresponding to a fading rate of 0.1% per cycle. Further inspection into the electrode morphology at pristine state and after 200 cycles is needed to understand the superior cycle performance.

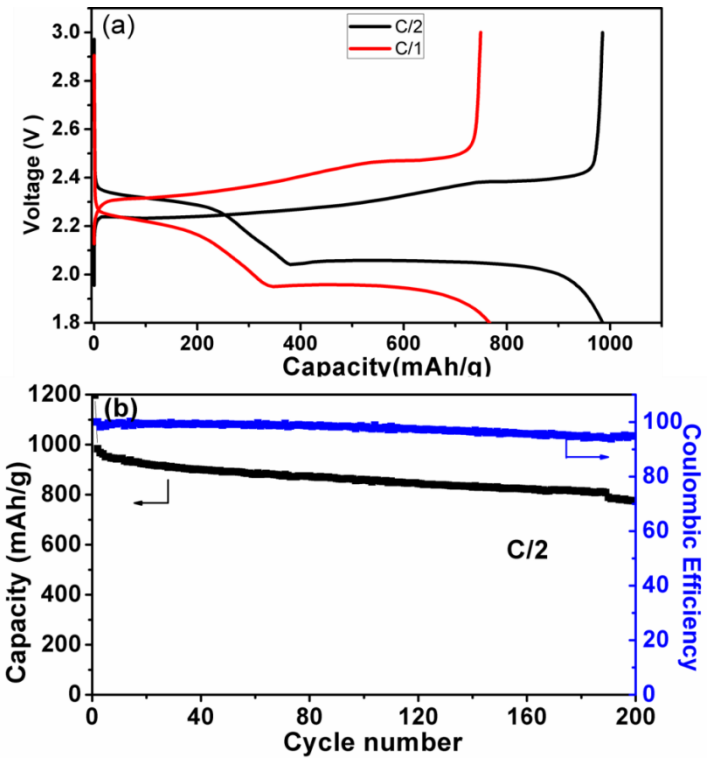

Figure 4.10 (a) Initial discharge/charge voltage profiles of nano-MgB_2/CNT/S-60 composite at C/2 and C, respectively. (b) The capacity retention of nano-MgB_2/CNT/S-60 composite at C/2 with corresponding Coulombic efficiency over 200 cycles.

4.4 Conclusion

Bulk and nanosized MgB_2 were successfully synthesized by thermal decomposition of $Mg(BH_4)_2$ and solid-state reaction between elements, respectively. The aim of this research is to look for a new class of sulfur host material that has both metallic

conductivity and capability to adsorb LiPS. In all forms of MgB_2 in this chapter, highly crystalline MgB_2 was formed as the dominant phase, but also with a minor phase of MgO on the surface. CNTs proved to be an effective additive to inhibit particle growth for solid-state reaction in this case. Nano-MgB_2/CNT, with the smallest particle size among synthesized MgB_2 was investigated as a sulfur host material in Li-S cell. With 60 wt% of sulfur, the cell was able to maintain 78.5 % of initial capacity over 200 cycles at C/2, with a capacity loss of 0.1% per cycle.

Future perspectives

The work presented in this thesis was focused on the positive electrode materials for Li-S battery. Currently, in order for a Li-S cell to operate with high specific capacity, rate capability and most importantly, prolonged cycle performance, the positive electrode is still the most challenging and hindered part. LiPS dissolution and shuttle phenomenon is considered to be a major factor and is the main problem to be solved in this thesis.

In the first part of the thesis, a mesoporous reduced titanium oxide with high surface area was synthesized and applied as a sulfur host for Li-S cell. It's bifunctional in providing metallic conductivity and adsorption for LiPSs. XPS study has confirmed the strong interaction between Li_2S_4 and Ti_4O_7, but further probing into this interaction for not only understanding the mechanism but also extending the concept to other metallic oxide materials is necessary. XANES and Raman spectroscopy can potentially provide more information and *ab initio* calculations based on DFT framework will be carried out on the interaction for further understanding. Other factors affecting electrochemical performances of Li-S cells, including volume expansion/contraction, Li_2S deposition and oxidation upon cycling should also be investigated to fully evaluate the function of Ti_4O_7. In addition, increasing the surface area of Ti_4O_7 and loading more sulfur is equally important in order to make it more practically applicable. With the aim of improving longer-term cycle performance, the development of multi-component electrodes where expansion/contraction can be controlled through the use of tailored binders will be explored in future work.

In the second part, the use of nanostructured MgB_2 to construct sulfur cathodes was explored. MgB_2 synthesized with the aid of CNTs additive exhibited the smallest particle size and the sulfur cathode thus made demonstrated superior capacity retention than bulk MgB_2. MgB_2 is similar with Ti_4O_7 in the sense of high conductivity and polar structure, but the polarity and chemical property of boride is different from oxide. The investigation into the interaction between MgB_2 and LiPSs via XPS and polysulfide adsorption studies and the comparison of MgB_2 with Ti_4O_7 in these aspects is in progress now. On the other hand, since MgB_2 is lighter than titanium oxides, it has potential to host more sulfur effectively, provided they have same architecture. Therefore future work will also be focused on synthesis of porous MgB_2 with higher surface area. Especially, one work to be explored is to synthesize MgB_2-coated CNTs composite, where B will be first deposited on CNTs via a chemical vapor deposition method, followed by reacting with Mg vapor to form MgB_2. This approach can take advantages of the flexibility and network construction attributed from CNTs, with synergetic benefits of alleviating expansion/contraction and LiPSs dissolution during cycling.

In order to commercialize Li-S battery, the anode and electrolyte need to be improved as well. With Li_2S as a cathode material instead of sulfur, there will be no need to use lithium metal anode to provide lithium. Novel anode materials with high specific capacity, like silicon or carbon can be explored in the future.

References

(1) Goodenough, J. B.; Kim, Y. *Chem. Mater.* **2010**, *22*, 587.

(2) Goodenough, J. B.; Park, K.-S. *J. Am. Chem. Soc.* **2013**, *135*, 1167.

(3) Tarascon, J. M.; Armand, M. *Nature* **2001**, *414*, 359.

(4) Mizushima, K.; Jones, P. C.; Wiseman, P. J.; Goodenough, J. B. *Mater. Res. Bull.* **1980**, *15*, 783.

(5) Bruce, P. G.; Freunberger, S. A.; Hardwick, L. J.; Tarascon, J. M. *Nat. Mater.* **2012**, *11*, 19.

(6) Oh, S. H.; Black, R.; Pomerantseva, E.; Lee, J. H.; Nazar, L. F. *Nat. Chem.* **2012**, *4*, 1004.

(7) Peng, Z.; Freunberger, S. A.; Chen, Y.; Bruce, P. G. *Science* **2012**, *337*, 563.

(8) Ottakam Thotiyl, M. M.; Freunberger, S. A.; Peng, Z.; Chen, Y.; Liu, Z.; Bruce, P. G. *Nat. Mater.* **2013**, *12*, 1050.

(9) Chen, Y.; Freunberger, S. A.; Peng, Z.; Fontaine, O.; Bruce, P. G. *Nat. Chem.* **2013**, *5*, 489.

(10) Cuisinier, M.; Cabelguen, P.-E.; Evers, S.; He, G.; Kolbeck, M.; Garsuch, A.; Bolin, T.; Balasubramanian, M.; Nazar, L. F. *J. Phy. Chem. Lett.* **2013**, *4*, 3227.

(11) Patel, M. U.; Arcon, I.; Aquilanti, G.; Stievano, L.; Mali, G.; Dominko, R. *Chemphyschem* **2014**. DOI: 10.1002/cphc.201300972.

(12) Patel, M. U.; Demir-Cakan, R.; Morcrette, M.; Tarascon, J. M.; Gaberscek, M.; Dominko, R. *ChemSusChem* **2013**, *6*, 1177.

(13) Nelson, J.; Misra, S.; Yang, Y.; Jackson, A.; Liu, Y.; Wang, H.; Dai, H.; Andrews, J. C.; Cui, Y.; Toney, M. F. *J. Am. Chem. Soc.* **2012**, *134*, 6337.

(14) Knoxville, T.; Dean, J.; McGraw-Hill, New York: 1999.

(15) Ji, X.; Lee, K. T.; Nazar, L. F. *Nat. Mater.* **2009**, *8*, 500.

(16) He, G.; Ji, X.; Nazar, L. *Energy Environ. Sci.* **2011**, *4*, 2878.

(17) Schuster, J.; He, G.; Mandlmeier, B.; Yim, T.; Lee, K. T.; Bein, T.; Nazar, L. F. *Angew. Chem. Int .Ed Engl.* **2012**, *51*, 3591.

(18) Jayaprakash, N.; Shen, J.; Moganty, S. S.; Corona, A.; Archer, L. A. *Angew. Chem. Int. Ed. Engl.* **2011**, *50*, 5904.

(19) He, G.; Evers, S.; Liang, X.; Cuisinier, M.; Garsuch, A.; Nazar, L. F. *ACS Nano* **2013**, *7*, 10920.

(20) Zhang, B.; Qin, X.; Li, G. R.; Gao, X. P. *Energy Environ. Sci.* **2010**, *3*, 1531.

(21) Xin, S.; Gu, L.; Zhao, N. H.; Yin, Y. X.; Zhou, L. J.; Guo, Y. G.; Wan, L. J. *J. Am. Chem. Soc.* **2012**, *134*, 18510.

(22) Wang, H.; Yang, Y.; Liang, Y.; Robinson, J. T.; Li, Y.; Jackson, A.; Cui, Y.; Dai, H. *Nano Lett.* **2011**, *11*, 2644.

(23) Xiao, M.; Huang, M.; Zeng, S.; Han, D.; Wang, S.; Sun, L.; Meng, Y. *RSC Adv.* **2013**, *3*, 4914.

(24) Evers, S.; Nazar, L. F. *Chem. Commun.* **2012**, *48*, 1233.

(25) Zhou, G.; Yin, L.-C.; Wang, D.-W.; Li, L.; Pei, S.; Gentle, I. R.; Li, F.; Cheng, H.-M. *ACS Nano* **2013**, *7*, 5367.

(26) Ji, L.; Rao, M.; Zheng, H.; Zhang, L.; Li, Y.; Duan, W.; Guo, J.; Cairns, E. J.; Zhang, Y. *J. Am. Chem. Soc.* **2011**, *133*, 18522.

(27) Song, M. K.; Zhang, Y.; Cairns, E. J. *Nano Lett.* **2013**.

(28) Zhou, W.; Chen, H.; Yu, Y.; Wang, D.; Cui, Z.; DiSalvo, F. J.; Abruña, H. D. *ACS Nano* **2013**, *7*, 8801.

(29) Zheng, G.; Zhang, Q.; Cha, J. J.; Yang, Y.; Li, W.; Seh, Z. W.; Cui, Y. *Nano Lett.* **2013**, *13*, 1265.

(30) Li, W.; Zheng, G.; Yang, Y.; Seh, Z. W.; Liu, N.; Cui, Y. *Proc. Natl. Acad. Sci. U.S.A.* **2013**, *110*, 7148.

(31) Chung, W. J.; Griebel, J. J.; Kim, E. T.; Yoon, H.; Simmonds, A. G.; Ji, H. J.; Dirlam, P. T.; Glass, R. S.; Wie, J. J.; Nguyen, N. A.; Guralnick, B. W.; Park, J.; Somogyi, A.; Theato, P.; Mackay, M. E.; Sung, Y. E.; Char, K.; Pyun, J. *Nat. Chem.* **2013**, *5*, 518.

(32) Zhou, W.; Yu, Y.; Chen, H.; DiSalvo, F. J.; Abruna, H. D. *J. Am. Chem. Soc.* **2013**, *135*, 16736.

(33) Guo, J.; Yang, Z.; Yu, Y.; Abruna, H. D.; Archer, L. A. *J. Am. Chem. Soc.* **2013**, *135*, 763.

(34) Xiao, L.; Cao, Y.; Xiao, J.; Schwenzer, B.; Engelhard, M. H.; Saraf, L. V.; Nie, Z.; Exarhos, G. J.; Liu, J. *Adv. Mater.* **2012**, *24*, 1176.

(35) Ji, X.; Evers, S.; Black, R.; Nazar, L. F. *Nat. Commun.* **2011**, *2*, 325.

(36) Evers, S.; Yim, T.; Nazar, L. F. *J. Phy. Chem. C* **2012**, *116*, 19653.

(37) Wei Seh, Z.; Li, W.; Cha, J. J.; Zheng, G.; Yang, Y.; McDowell, M. T.; Hsu, P. C.; Cui, Y. *Nat. Commun.* **2013**, *4*, 1331.

(38) Lee, K. T.; Black, R.; Yim, T.; Ji, X.; Nazar, L. F. *Adv.Eng. Mater.s* **2012**, *2*, 1490.

(39) Agostini, M.; Aihara, Y.; Yamada, T.; Scrosati, B.; Hassoun, J. *Solid State Ionics* **2013**, *244*, 48.

(40) Gao, J.; Lowe, M. A.; Kiya, Y.; Abruña, H. D. *J. Phy.Chem. C* **2011**, *115*, 25132.

(41) Dokko, K.; Tachikawa, N.; Yamauchi, K.; Tsuchiya, M.; Yamazaki, A.; Takashima, E.; Park, J. W.; Ueno, K.; Seki, S.; Serizawa, N.; Watanabe, M. *J. Electrochem. Soc.* **2013**, *160*, A1304.

(42) Suo, L.; Hu, Y. S.; Li, H.; Armand, M.; Chen, L. *Nat. Commun.* **2013**, *4*, 1481.

(43) Cheng, X.-B.; Huang, J.-Q.; Peng, H.-J.; Nie, J.-Q.; Liu, X.-Y.; Zhang, Q.; Wei, F. *J. Power Sources* **2014**, *253*, 263.

(44) Su, Y.-S.; Manthiram, A. *Nat. Commun.* **2012**, *3*, 1166.

(45) Huang, J.-Q.; Zhang, Q.; Peng, H.-J.; Liu, X.-Y.; Qian, W.-Z.; Wei, F. *Energy Environ. Sci.* **2014**,,**7**, 347-353

(46) Aurbach, D.; Pollak, E.; Elazari, R.; Salitra, G.; Kelley, C. S.; Affinito, J. *J. Electrochem. Soc.* **2009**, *156*, A694.

(47) Lin, Z.; Liu, Z.; Fu, W.; Dudney, N. J.; Liang, C. *Adv. Funct. Mater.* **2013**, *23*, 1064.

(48) Huang, C.; Xiao, J.; Shao, Y.; Zheng, J.; Bennett, W. D.; Lu, D.; Laxmikant, S. V.; Engelhard, M.; Ji, L.; Zhang, J.; Li, X.; Graff, G. L.; Liu, J. *Nat. Commun.* **2014**, *5*, 3015.

(49) Herbert, D.; Ulam, J. *German Patent* **1962**, *1*.

(50) http://hyperphysics.phy-astr.gsu.edu/hbase/quantum/bragg.html

(51) Cabelguen, P.-E. (2013) Advanced research on Lithium-Sulfur batteries: studies of lithium polysulfides. M. Sc. Thesis. University of Waterloo, Canada.

(52) Zhou, G.; Pei, S.; Li, L.; Wang, D.-W.; Wang, S.; Huang, K.; Yin, L.-C.; Li, F.; Cheng, H.-M. *Adv. Mater.* **2013**, DOI: 10.1002/adma.201302877.

(53) Kim, H.; Lee, J. T.; Lee, D.-C.; Magasinski, A.; Cho, W.-i.; Yushin, G. *Adv. Eng. Mater.* **2013**, *3*, 1308.

(54) Smith, J. R.; Walsh, F. C.; Clarke, R. L. *J. Appl. Electrochem.* **1998**, *28*, 1021.

(55) Yao, C.; Li, F.; Li, X.; Xia, D. *J. Mater. Chem.* **2012**, *22*, 16560.

(56) Kartio, I. J.; Basilio, C. I.; Yoon, R. H. *Langmuir* **1998**, *14*, 5274.

(57) Moulder, J. F.; Stickle, W. F., Sobol, P. E. and Bomben, K. D. Handbook of X-ray Photoelectron Spectroscopy; Perkin-Elmer Corporation:Eden Prairie, MN, 1992.

(58) Deng, Z.; Zhang, Z.; Lai, Y.; Liu, J.; Li, J.; Liu, Y. *J. Electrochem. Soc.* **2013**, *160*, A553.

(59) Pang, Q.; Dipan, K.; Cuisinier, M.; Nazar, L. **2014**, *submitted*.

(60) Kortus, J.; Mazin, I. I.; Belashchenko, K. D.; Antropov, V. P.; Boyer, L. L. *Phy. Rev. Lett.* **2001**, *86*, 4656.

(61) Mazin, I. I.; Antropov, V. P. *Physica C: Superconduc.***2003**, *385*, 49.

(62) Despoja, V.; Mowbray, D. J.; Silkin, V. M. *Phys. Rev. B* **2011**, *84*, 104514.

(63) Schneider, M.; Lipp, D.; Gladun, A.; Zahn, P.; Handstein, A.; Fuchs, G.; Drechsler, S.-L.; Richter, M.; Müller, K.-H.; Rosner, H. *Physica C: Superconduc.***2001**, *363*, 6.

(64) Bud'Ko, S.; Lapertot, G.; Petrovic, C.; Cunningham, C.; Anderson, N.; Canfield, P. *Phy.Rev. Lett.* **2001**, *86*, 1877.

(65) Ko, J.-W.; Yoo, J.; Kim, Y.-K.; Chung, S. J.; Yoo, S. I. *Physica C: Superconduc.* **2004**, *412-414*, 1194.

(66) Nath, M.; Parkinson, B. A. *Adv.Mater.* **2006**, *18*, 1865.

(67) Yang, J.; Zheng, J.; Zhang, X.; Li, Y.; Yang, R.; Feng, Q.; Li, X. *Chem. Commun.***2010**, *46*, 7530.

(68) Wu, Y.; Messer, B.; Yang, P. *Adv. Mater.* **2001**, *13*, 1487.

(69) Vasquez, R.; Jung, C.; Park, M.-S.; Kim, H.-J.; Kim, J.; Lee, S.-I. *Phy. Rev. B* **2001**, *64*, 052510.

(70) Talapatra, A.; Bandyopadhyay, S.; Sen, P.; Barat, P.; Mukherjee, S.; Mukherjee, M. *Physica C: Superconduc.* **2005**, *419*, 141.

(71) Song, M.-S.; Han, S.-C.; Kim, H.-S.; Kim, J.-H.; Kim, K.-T.; Kang, Y.-M.; Ahn, H.-J.; Dou, S. X.; Lee, J.-Y. *J. Electrochem. Soc.* **2004**, *151*, A791.